



Cite this: *Nanoscale Horiz.*, 2024,
9, 186

Tumor microenvironment-responsive degradable silica nanoparticles: design principles and precision theranostic applications

Junjie Zhang,^{†*} Kaiyuan Tang,[†] Zilu Liu,^a Zhijing Zhang,^a Shufan Duan,^a
Hui Wang,^a Hui Yang,^a Dongliang Yang^{†*} and Wenpei Fan^{†*}

Silica nanoparticles have emerged as promising candidates in the field of nanomedicine due to their remarkable versatility and customizable properties. However, concerns about their potential toxicity in healthy tissues and organs have hindered their widespread clinical translation. To address this challenge, significant attention has been directed toward a specific subset of silica nanoparticles, namely degradable silica nanoparticles, primarily because of their excellent biocompatibility and responsive biodegradability. In this review, we provide a comprehensive understanding of degradable silica nanoparticles, categorizing them into two distinct groups: inorganic species-doped and organic moiety-doped silica nanoparticles based on their framework components. Next, the recent progress of tumor microenvironment (TME)-responsive degradable silica nanoparticles for precision theranostic applications is summarized in detail. Finally, current bottlenecks and future opportunities of theranostic nanomedicines based on degradable silica nanoparticles in clinical applications are also outlined and discussed. The aim of this comprehensive review is to shed light on the potential of degradable silica nanoparticles in addressing current challenges in nanomedicine, offering insights into their design, applications in tumor diagnosis and treatment, and paving the way for future advancements in clinical theranostic nanomedicines.

Received 6th September 2023,
Accepted 28th November 2023

DOI: 10.1039/d3nh00388d

rsc.li/nanoscale-horizons

^a School of Fundamental Sciences, Bengbu Medical College, Bengbu 233030, P. R. China. E-mail: zhangjj@bbmc.edu.cn

^b State Key Laboratory of Organic Electronics and Information Displays & Institute of Advanced Materials (IAM), Nanjing University of Posts & Telecommunications, 9 Wenyuan Road, Nanjing 210023, P. R. China

^c Nanjing Polytechnic Institute, Nanjing 210048, P. R. China. E-mail: yangdl1023@njtech.edu.cn

^d State Key Laboratory of Natural Medicines and Jiangsu Key Laboratory of Drug Discovery for Metabolic Diseases, Center of Advanced Pharmaceuticals and Biomaterials, China Pharmaceutical University, Nanjing 211198, P. R. China. E-mail: wenpei.fan@cpu.edu.cn

[†] These authors have contributed equally to this work.



Junjie Zhang

Junjie Zhang received her PhD degree from Nanjing University of Posts and Telecommunications under the supervision of Professor Lianhui Wang in 2020. Currently, she is an assistant professor at the School of Fundamental Sciences, Bengbu Medical College. Her research interest focuses on the design and synthesis of multifunctional nanotheranostics for multimodal imaging guided synergistic therapy.



Kaiyuan Tang

Kaiyuan Tang joined Bengbu Medical College in 2020 to pursue a bachelor's degree in Medical Imaging. In 2021, he joined Dr Zhang Junjie's research group, focusing on the design and synthesis of multifunctional nanotherapeutics for multimodal imaging-guided collaborative therapies.

1. Introduction

Cancer is a major global cause of death, posing a serious threat to public health and safety.¹ It is characterized by abnormal cell proliferation and tumor formation resulting from gene mutations, ultimately leading to secondary metastases. Unlike healthy cells, which maintain a dynamic equilibrium in the surrounding tissue environment through cell proliferation, differentiation, and apoptosis, tumor cells undergo rapid and uncontrolled proliferation, giving rise to a malignant tumor microenvironment (TME).^{2–6} The TME is a dynamic microenvironment comprising both tumor cells and nontumor cells, including blood vessels, stroma, endothelial cells, and immune cells. It exhibits distinctive features, such as dynamic hypoxia, high concentrations of redox components, elevated intracellular adenosine triphosphate (ATP) and lactate levels, and extracellular acidosis.^{6–13} Additionally, certain types of tumors possess specific microenvironments. Vascular tumors are characterized by vascular leakage, chaotic branching of blood vessels, uneven blood flow distribution, and high stromal fluid pressure, while stromal tumors present prominent features of abnormal tumor-associated fibroblasts and a dense extracellular matrix.^{14,15} Unrestrained growth and dissemination of cancer cells lead to their remarkable heterogeneity and resistance, allowing them to evade immune surveillance, rendering conventional cancer treatment approaches (*e.g.*, surgery, chemotherapy (CMT), radiotherapy (RT), *etc.*) relatively ineffective and often accompanied by severe side effects.^{16–18} Consequently, there is an urgent need to develop precise cancer-specific treatment methods that not only eradicate tumors but also minimize toxic side effects.

In recent years, nanotechnology has garnered growing interest in the field of cancer diagnosis and treatment, leading to a heightened focus on the utilization of nanomaterials in the field of nanomedicine. Nanomedicine utilizes nanomaterials to accumulate in tumor tissues through the enhanced permeability and retention (EPR) effect, leading to enhanced treatment efficacy.^{19,20} Moreover, certain organic or inorganic

nanomaterials, such as silica, polymers, proteins, and metal oxides, are designed to load drugs, proteins, enzymes, RNA, and other molecules, thereby enhancing the utilization and effectiveness of therapeutics.^{21–23} Although using nanomaterials to deliver small-molecule therapeutic drugs can significantly reduce their interactions with normal tissues and thus decrease toxic side effects, there remains a risk of drug leakage, challenging the safety of the treatment. The proposal of stimuli-responsive therapy has enabled the design of nanomaterials to specifically respond to the TME, leading to various beneficial conformational changes, such as carrier decomposition, ligand exposure, and component disassembly.^{5,24,25} This unique treatment mechanism leverages nanomaterials to protect drugs, thereby avoiding nonspecific interactions with healthy tissues and achieving excellent diagnostic and therapeutic effects.

The practical clinical applications of nanomaterials are limited by their potential toxicity within the body and their slow biological clearance rate.²⁶ Research has shown that many types of nanomaterials are nondegradable under biological conditions but can be safely excreted through renal glomerular filtration due to their small size below the typical 5.5 nm renal clearance threshold.^{27–29} Nevertheless, nanomaterials with sizes exceeding 10 nm may be captured and absorbed by the reticuloendothelial system (RES), raising concerns about potential long-term toxicity.^{30,31} Additionally, most inorganic nanoparticles are nonbiodegradable or have long degradation periods, and some degradation byproducts from heavy metal oxides, such as mercury ions, can cause significant harm to the human body.^{32,33} The degradation of organic nanoparticles is influenced by factors such as organic components, hydrophobicity, and molecular weight, potentially posing hazards to the body.²⁶ As a result, researchers are focusing on nanomaterials with rapid degradability and biological safety.

Silicon, an abundant element on Earth and a rich trace element in the human body, plays a crucial role in the body's metabolic processes. Silicon substances ingested by the body



Dongliang Yang

Dongliang Yang received his PhD degree from the Nanjing University of Posts and Telecommunications. He is currently an associate professor at the School of Physical and Mathematical Sciences, Nanjing Tech University. His research is primarily focused on nanomedicine, particularly the development of light-functional materials for the treatment of drug-resistant bacterial infections.



Wenpei Fan

Prof. Wenpei Fan received his PhD in 2015 from the Shanghai Institute of Ceramics, Chinese Academy of Sciences. During 2015–2019, he worked at the National Institutes of Health (USA) as a postdoctoral fellow. Since November 2019, he has been a full professor at the Center of Advanced Pharmaceuticals and Biomaterials, China Pharmaceutical University. He has published over 80 papers in reputed journals. His research interests focus

on the design and synthesis of multifunctional theranostic nanomedicines for drug delivery, multimodal imaging, and precision synergistic therapy.

can circulate in blood plasma, being absorbed in the form of silicic acid and excreted through urine, thus providing robust assurance for human health safety.^{34,35} As a result, silicon-based nanomaterials have received widespread attention in research. Among these materials, silica nanoparticles, as representative silicon-based nanomaterials, serve as versatile carriers for a wide range of disease diagnosis and treatment applications due to their stable surface silanol groups that facilitate numerous surface chemical reactions.^{36,37} Silica nanoparticles exhibit various configurations, including nonporous, mesoporous, hollow, and core-shell structures, with abundant surface silanes, significantly aiding drug loading and the construction of TME-responsive systems.^{38,39} Among these, the degradation ability of silica nanoparticles is of particular attention. This is due to the tightly packed Si–O–Si structure within silica nanoparticles, which leads to slow degradation within the biological system and may result in their accumulation, causing tissue and organ damage and even systemic toxicity.^{40–43} In recent years, research findings have indicated that silica nanoparticles can be combined with inorganic or organic components, further optimizing their tumor therapeutic and biodegradable capabilities and significantly advancing the development of TME-responsive degradable materials.^{26,44–46} The outstanding degradability of silica nanoparticles not only enables efficient clearance and low toxicity but also allows precise control of drug release, thereby enhancing therapeutic efficacy.⁴⁷ These degradable silica nanoparticles can be tailored in terms of particle size and morphology, exhibit excellent biocompatibility, and demonstrate high cellular uptake rates, making them highly attractive for tumor imaging and treatment. Incorporating imaging agents or drugs into degradable silica nanoparticles or surface modification of nanocarriers facilitates the design of TME-responsive nanoprobe, capitalizing on the distinctions between the tumor and normal tissues for precise tumor diagnosis and drug release.⁴⁸ Furthermore, soft organosilica nanoparticles not only extend the blood circulation time but also facilitate effective drug accumulation within tumor cells.⁴⁹ Additionally, appropriate surface functionalization prevents interactions between nanocomposites and blood components or the endothelial system, thereby increasing drug utilization.⁵⁰

Over the last decade, significant advancements have been achieved in the progressive development and fine-tuning of degradable silica nanoparticles meticulously designed for therapeutic and imaging applications, with a specific focus on targeting the intricate and dynamic TME. However, there is still no comprehensive review centered explicitly on TME-responsive precision theranostic applications rooted in the utilization of degradable silica nanoparticles. In this paper, an exhaustive exploration encompassing the synthesis and meticulous classification of degradable silica nanoparticles is undertaken. A meticulous examination of a gamut of TME-specific responses that have been unveiled in recent years is carried out. Simultaneously, sagacious analysis is conducted, delving into the inherent potential opportunities and multifaceted challenges that underlie the strategic harnessing of

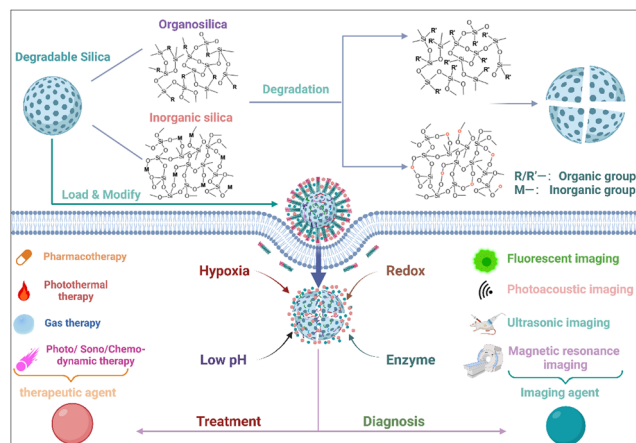


Fig. 1 Schematic illustration of TME-responsive precision theranostic applications that are based on the utilization of degradable silica nanoparticles. Copyright from biorender.

degradable silica nanoparticles, thereby fostering precision-centric diagnostics and therapeutics within the practical realms of clinical applications (Fig. 1).

2. Classification of degradable silica nanoparticles

Silica nanoparticles have garnered extensive attention and application in biomedical research due to their large surface area and adjustable physical/chemical properties. Nevertheless, the slow degradation and extended degradation period of silica raise concerns about potential long-term and latent pathogenic effects in physiological systems.^{51,52} Therefore, it is imperative to regulate the degradation of silica nanoparticles to ensure their safe application in living organisms. Studies have reported that silica nanoparticles rapidly dissolve into silicic acid through continuous hydration, hydrolysis, and ion exchange processes, with the dissolution rate dependent on the degradation medium and system saturation.^{53,54} Thus, reducing the accumulation of silicic acid degradation products can effectively accelerate the degradation of silica nanoparticles in physiological settings.

Developing degradable silica nanoparticles that rapidly degrade in the body is a promising approach, enhancing their safety and efficiency for biomedical applications. When inside the body, degradable silica nanoparticles respond to the biological environment, including fluid temperature, pH, and enzyme activity, catalyzing the degradation rate and breaking the material down into small molecular compounds that are eventually absorbed or excreted through metabolic pathways.^{26,55,56} In this review, we categorize degradable silica based on its framework components into inorganic or organic silica nanoparticles and extensively detail their synthesis methods and degradation behaviours.

2.1. Inorganic species-doped silica nanoparticles

The hydrolysis of silica nanoparticles is a multifaceted process influenced by a plethora of factors, including size, morphology,

pore size, and surface functionalization, as well as reaction temperature, concentration, pH, and pressure, all of which collectively contribute to the intricacies of this reaction.^{26,57–59} Under ideal conditions, the fundamental chemistry of silica nanoparticle hydrolysis in an aqueous environment can be succinctly described as the hydration of silica nanoparticles through interaction with adsorbed water molecules, resulting in the creation of multiple silanol groups. These silanol groups subsequently engage in ion exchange reactions, liberating silicic acid, while the remaining silanol groups persist in their interactions with water, facilitating the ongoing degradation process. As this process unfolds, the strength of silicon–oxygen bonds within the silicon-based nanomaterial gradually diminishes, ultimately leading to the structural collapse of the material.^{57,60} Consequently, the degradation of the silica framework can be controlled by adjusting the content of degradable organic groups or modifying the strength of the silica framework through a synthetic process.^{46,61} Introducing metal ions into the framework of silica at the molecular level can alter its inherent physicochemical properties. In physiological environments, metals can interact with specific substances, prompting detachment from the silica framework and resulting in a substantial number of defects in the material structure, which enhances the opportunities for water molecules to react with other silicon atoms, thereby accelerating the aforementioned degradation.^{62,63} Metals are typically integrated into the silicate network through two distinct mechanisms. In one approach, they establish a direct linkage with silicon hydroxyl groups *via* Si–O–M bonds, yielding compounds with uniform characteristics. An exemplary illustration of this phenomenon is observed in the diverse array of silicate minerals. The alternative mode of integration entails their incorporation within the network as elements, salts, oxide clusters, or nanoparticles. A wealth of scholarly studies underscores that the introduction of metal ions such as calcium, iron, and manganese not only affords the ability to regulate material stability but also furnishes catalytic and coordination sites that accelerate the hydrolysis of the silica network.^{63,64} This infusion of supplementary attributes and functionalities enhances the inherent potential of the pristine siloxane matrix, rendering it pertinent across a broad spectrum of domains, including medical imaging and disease treatment (Fig. 2).

2.1.1. Iron. Iron is an essential trace element for the human body, and the incorporation of iron into the silica framework allows for tailoring the behaviour and reactivity of

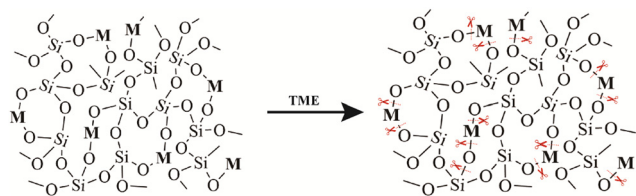


Fig. 2 Diagram illustrating the degradation mechanism of the metal ion-doped silica nanoparticles.

silica nanoparticles, opening up new avenues for designing advanced nanomaterials with desired properties. Wang *et al.* utilized a sol–gel method to synthesize monodisperse iron-containing hollow mesoporous silica nanoparticles (rFeOx-HMSN) *via* a “dissolution–regeneration” strategy.⁴⁴ They employed a sequential approach to synthesize monodisperse mesoporous silica nanoparticles (MSNs) utilizing cetyltrimethylammonium bromide (CTAC), triethanolamine (TEA) and tetraethyl orthosilicate (TEOS). Subsequently, the core underwent etching under urea-induced alkaline conditions to yield a hollow architecture. Meanwhile, Fe(acac)₃ self-assembled with silica oligomers, yielding hollow mesoporous silica nanoparticles embedded in iron-containing frameworks (Fe^{III}-HMSN). The robust coordination between iron ions and proteins facilitated the collapse of the iron–silica framework in protein-rich tissue environments, inducing structural defects within the silica framework and thereby enhancing the biodegradability of silica nanoparticles (Fig. 3a). To further enhance the catalytic efficiency of iron in the Fenton reaction, Fe^{III}-HMSN was subsequently subjected to reduction in an H₂/Ar atmosphere, yielding Fe^{II}-containing HMSN (rFeOx-HMSN). *In vitro* degradation studies of rFeOx-HMSN revealed its structural stability in neutral fetal bovine serum for up to 1 day, while complete degradation occurred within 7 days. The biodegradation process of the nanocatalyst commenced on the third day after uptake by 4T1 tumor cells, with irregular fragments observed on the 7th day (Fig. 3b). Nevertheless, prolonged exposure to elevated iron ion concentrations raises concerns regarding potential cardiovascular toxicity, underscoring the

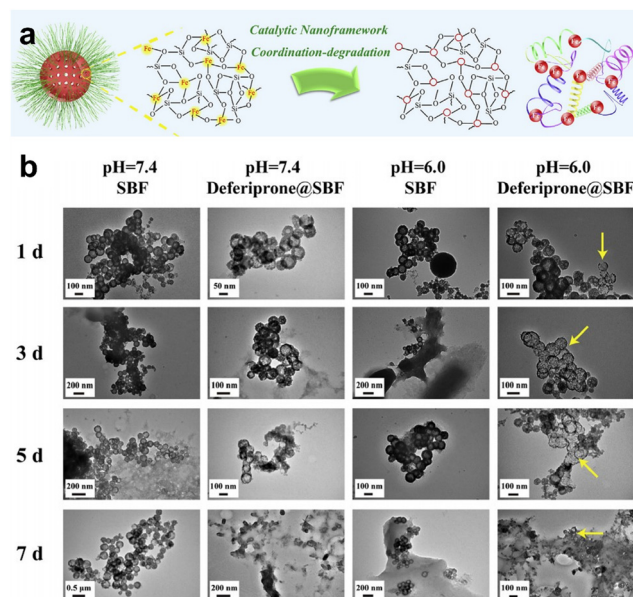


Fig. 3 (a) Diagram illustrating the degradation mechanism of the rFeOx-HMSN nanocatalyst. (b) TEM images visually capturing the progressive degradation of rFeOx-HMSNs across diverse simulated body fluid environments. Reproduced from ref. 44 with permission from Elsevier, copyright 2018.

need for ongoing monitoring of the iron–silica framework over extended periods.

2.1.2. Magnesium. Given its high biocompatibility and abundance within the human body, magnesium has emerged as an optimal metal for engineering silica frameworks. In the study conducted by Yu *et al.*, highly dispersed MSNs were synthesized using the sol–gel method. To produce hollow mesoporous magnesium silicate nanoparticles (HMMSNs), the core etching and surface deposition of magnesium salt onto the MSNs were successfully accomplished through the utilization of an alkaline ammonia solution and magnesium chloride, as depicted in Fig. 4a.⁶⁵ During this transformative process, the silica shell gradually evolved into a magnesium–silicate framework. This framework exhibited the capability to undergo degradation and release Mg^{2+} ions within the acidic TME, leading to the introduction of structural defects in the chemical composition. Experimental investigations involving exposure of HMMSNs to SBF with pH levels of 5.5, 6.8 and 7.4 demonstrated significant structural alterations (Fig. 4b). The SEM images of HMMSNs during the biodegradation process exhibited complete structural breakdown within 48 h, leaving only very minute degradation fragments after 7 days. Inductively coupled plasma emission spectrometry (ICP-OES) quantitatively monitored the degradation process, revealing a clear pH-dependent release of magnesium and silicon ions from HMMSNs. Furthermore, HMMSNs exhibited the ability to maintain their intact structure during cellular uptake by 4T1 cells. Subsequently, substantial biodegradation of the nanostructures within the HMMSNs was observed on the second day: central nanoparticle structures displayed rupture, and most nanoparticle shells underwent thinning. After 7 days of incubation, only residual biodegraded fragments of HMMSNs were discernible within the cells.

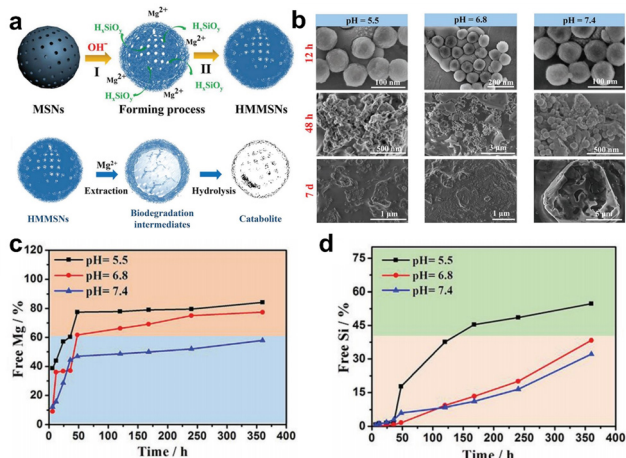


Fig. 4 (a) Schematic diagram of the synthesis and degradation of HMMSNs. (b) SEM was utilized for the characterization of the *in vitro* degradation process of HMMSNs. These images depict HMMSNs following their biodegradation in SBF solutions at three distinct pH levels. The content of (c) Mg and (d) Si components in SBF following exposure to different pH levels. Reproduced from ref. 65 with permission from Wiley, copyright 2018.

2.1.3. Manganese. Manganese, an indispensable element for human metabolism, is effectively regulated by the physiological intake and excretion system, exhibiting not only low toxicity but also remarkable biocompatibility. In a pioneering effort, Yu *et al.* devised a TME-responsive “manganese extraction” approach by fabricating manganese-doped hollow and microporous silica nanoparticles (Mn-HMSNs) through a meticulously tailored sol–gel process (Fig. 5a).⁶⁶ This innovative design not only augments the biodegradation of Mn-HMSNs but also expedites the cleavage of Si–O–Si bonds within their framework. The expedited release of manganese ions from Mn-HMSNs instigates an accelerated liberation of silicon ions from the carriers, particularly evident in SBF at pH 5.0 (Fig. 5b). Impressively, the TEM imagery vividly portrays a substantial transformation in the architecture of Mn-HMSNs after a mere 6 h incubation in an acidic SBF milieu, culminating in near-complete disintegration after 48 h. Furthermore, in a GSH-enriched SBF milieu, the nanostructures experience rapid fragmentation within a brief 6 h span, with the synergistic acidic environment further catalyzing the degradation pace. Profound insight into the biodegradation of Mn-HMSNs comes to light, as we observed discernible signs of degradation at 48 h post uptake by cancer cells. Notably, intracellular biodegradation, progressing on the third day, unveils a conspicuous fusion of degradation products, ultimately culminating in complete degradation on the seventh day. Additionally, Tao *et al.*⁶⁷ dispersed ethyleneimine polymer-modified mesoporous organic nanoparticles (MONs-PEI) in MnO_4^- solution and employed oleic acid (OA) elution to synthesize spherical and mechanically tunable manganese oxide-hybridized mesoporous silica nano-platforms (MMONs) for highly efficient tumor therapy. This achievement was realized through an *in situ* redox reaction between MnO_4^- and Si–O. The presence of Mn–O bonds allowed the Young’s modulus of the MMONs to be reduced from 790 MPa to 84.5 MPa. Soft nanoparticles with a low

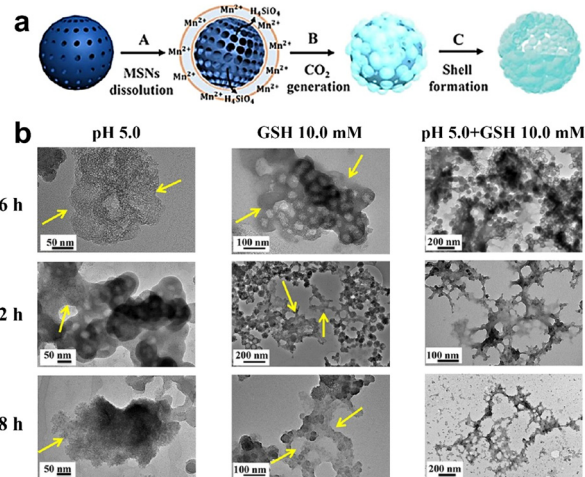


Fig. 5 (a) Schematic representation depicting the synthesis process of Mn-HMSNs. (b) Degradation of Mn-HMSNs influenced by pH and GSH concentrations. Reproduced from ref. 66 with permission from ACS, copyright 2016.

Young's modulus facilitate enhanced cellular uptake and tumor penetration but are susceptible to liver accumulation and macrophage capture. In contrast, hard nanoparticles exhibit low macrophage internalization and liver distribution, which is advantageous for prolonged blood circulation and effective tumor accumulation. Mechanically tunable nanoparticles integrate the advantages of both soft and hard nanoparticles, enabling the efficient delivery of therapeutic agents to tumor cells for precise tumor treatment. *In vivo* experiments demonstrated that, compared to their counterparts of soft MONs and stiff MONs, MMONs exhibited a 3.79- and 2.90-fold reduction in nonspecific liver distribution, along with a 2.87- and 1.83-fold increase in tumor accumulation, respectively.

2.1.4. Calcium. Calcium is an indispensable trace element that is vital for human metabolism and is ubiquitously found within living organisms. Consequently, the integration of calcium into the silica framework holds the potential to elevate the material's biocompatibility, mitigate biological toxicity, and bolster the stability and receptiveness of the material within biological systems. He *et al.* ingeniously incorporated calcium phosphate (CAP) into the synthesis of MSNs, yielding a novel hybrid drug carrier system (MS-CAP).⁶⁸ This innovative approach led to the creation of nanocarriers that exhibited rapid pH-responsive degradation behaviour, as depicted in Fig. 6a. The dissolution of CAP within the composite structure triggers the liberation of Ca^{2+} ions from the Si–O–Ca framework, instigating the formation of structural flaws. This Ca^{2+} release event was accompanied by the emergence of a multitude of nonbridging oxygen atoms, thereby augmenting nucleophilic attack sites for $\bullet\text{OH}$. Consequently, this process initiated the gradual dissolution of the silica component, thereby promoting the biodegradation of MS-CAP. TEM images obtained from SBF experiments vividly illustrated the erosion and irregular morphology changes in MS-CAP nanoparticles after just 4 h of exposure to PBS at pH 4.5. Subsequently, within 8 h, the nanoparticle structure experienced complete disintegration, fragmenting into small fragments measuring 10–20 nm. Upon reaching 24 h, only faint remnants remained, indicating near-complete degradation. Detailed quantification *via* ICP-OES revealed the extent of Ca^{2+} ion release from MS-CAP under varying pH conditions. Specifically, after 48 h of incubation in PBS at pH 4.5, 5.5, 6.5, and 7.4, MS-CAP released 98.84%, 80.23%, 18.49%, and 12.53% of its Ca^{2+} content, respectively. These findings underscored the exceptional stability of MS-CAP in neutral and mildly acidic environments, in contrast to its pronounced biodegradability under strongly acidic conditions. Furthermore, Kang *et al.* employed a hydrothermal method to fabricate a silica/hydroxyapatite hybrid carrier loaded with DOX (DOX@MSNs/HAP) (Fig. 6b).⁶⁹ The DOX release profile and TEM images of the nanoparticles revealed that under neutral conditions (pH 7.4), the nanoparticles maintained their structural integrity with limited drug release. In contrast, when exposed to acidic conditions (pH 6.5 and 5.5), the nanoparticles underwent gradual degradation, resulting in the formation of smaller structures and subsequent DOX release (Fig. 6c and d).

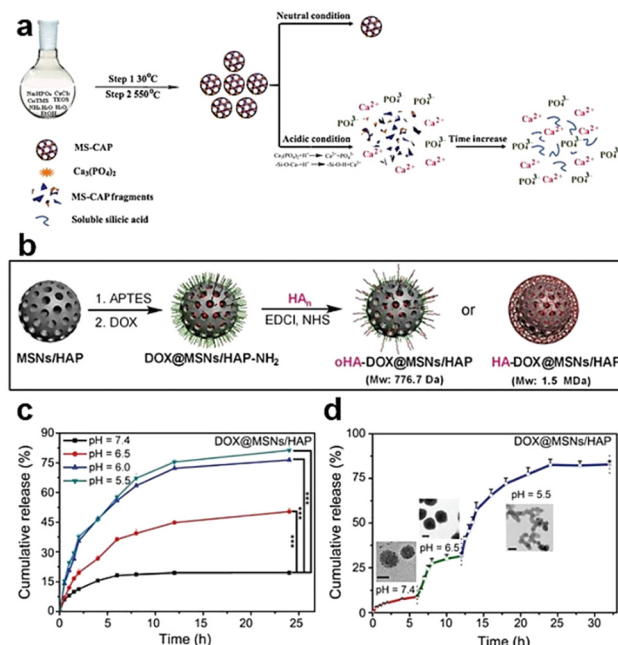


Fig. 6 (a) Schematic depiction of the synthesis and degradation process for MS-CAP. Reproduced from ref. 68 with permission from ACS, copyright 2017. (b) Schematic representation of the assembly of MSN/HAP and HA-DOX@MSN/HAP nanoplateforms. (c) Release profiles of DOX from DOX@MSNs/HAP in PBS buffer at varying pH values. (d) DOX release profiles from DOX@MSNs/HAP at different pH values, accompanied by TEM images captured after 4, 10, and 24 h of incubation. Reproduced from ref. 69 with permission from Wiley, copyright 2019.

This degradation behaviour was attributed to the presence of hydroxyapatite (HAP) within the silica structure. Furthermore, complexometric titration using EDTA confirmed a substantial release of Ca^{2+} from the hybrid nanoparticles in acidic solutions (pH 5.5 and 6.5), providing additional evidence for the degradation of the silica platform under acidic pH conditions.

2.1.5. Holmium. Holmium (Ho) is a rare-earth element that exhibits fluorescence properties under specific conditions, making it suitable for bioimaging and labelling purposes. Introducing holmium doping into the silica framework can confer fluorescence functionality to the material, potentially turning it into a fluorescent probe or labelling agent for tracking cellular, tissue, or biological activities. Furthermore, Ho possesses excellent biocompatibility and low toxicity, enhancing the safe application of the material *in vivo*. Wang *et al.* employed a modified Stöber method to synthesize uniform silica nanoparticles. Subsequently, Ho-doped hollow mesoporous silica nanospheres (Ho-HSNs) were hydrothermally produced in the presence of sodium acetate and holmium nitrate (Fig. 7).⁷⁰ The incorporation of Ho facilitated rapid degradation of Ho-HSNs within a slightly acidic and GSH-rich TME. PEG-modified Ho-HSNs were introduced into an acidic SBF with a pH of 5.2, resulting in the formation of aggregates on the nanosphere surface after 6 h of incubation. After 48 h of incubation in the acidic solution, most of the hollow structure of Ho-HSNs was completely disrupted, while under neutral conditions, no significant changes in their

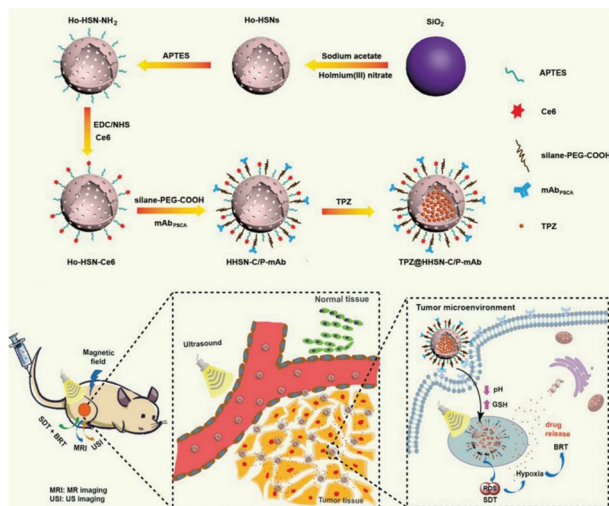


Fig. 7 Biological applications of the degradable Ho-HSN nanoplatform. Reproduced from ref. 70 with permission from Wiley, copyright 2018.

hollow structure were observed. This underscored the sustained degradability of Ho-HSN-PEG in an acidic environment. Furthermore, incubation in a GSH solution (10×10^{-3} M) for 6 h led to the collapse of the hollow mesoporous structure. To gain deeper insights into the biodegradation behaviour of Ho-HSN, Bio-TEM was employed to monitor the interaction between Ho-HSN-PEG and human prostate cancer (PC-3) cells during incubation. Initially, cancer cells internalized Ho-HSN-PEG, which accumulated in the cytoplasm. After 24 h of cellular uptake, alterations in nanomaterial morphology and structure became apparent. On the third day, significant degradation induced by the cellular microenvironment was observed, resulting in the absence of distinct spherical structures. On the fifth day, the remnants of the material within the cells had notably diminished, suggesting that the biodegradation byproducts were efficiently cleared by the cells.

2.2. Organic moiety-doped silica nanoparticles

The synthesis of monodisperse silica nanoparticles involves silica precursors such as TEOS and tetramethyl orthosilicate (TMOS), whereas organosilica nanoparticles require additional organosilica precursors during preparation.⁷¹ Organosilica nanoparticles can be classified into two types: periodically mesoporous organosilica composed entirely of organosilica precursors and organic-inorganic hybrid mesoporous silica nanoparticles comprising partly organic groups.^{62,72,73} Both types of organosilica nanoparticles utilize structure-directing agents, such as CTAB and CTAC, during the condensation process of bis-silane units $(R'O)_3Si-R-Si(OR')_3$. Herein, $R'O$ typically represents methoxy or ethoxy, while R denotes organic functional linkages between silicon atoms. The robustness of the silicon-carbon bonds (Si-C) and the hydrophobic interactions stemming from organic moieties collectively contribute to the exceptional stability exhibited by the passive alkane-bridged silica network within aqueous surroundings.²⁶ The introduction of organic bridges could substantially bolster the stability

of silica nanoparticles within aqueous phases. However, it concurrently imparts susceptibility to degradation when these silica nanoparticles are subjected to organic solvents. As a result, regulating and controlling the incorporation of organic components into silica nanoparticles allows for degradable organosilica with specific functions. The main methods for achieving this are the incorporation of easily degradable organic covalent groups or cleavable organosiloxanes.^{26,62,74} Different types of organic bridges (R) containing easily hydrolysed groups and reactive functional groups can be introduced into mesoporous organosilica nanoparticles to significantly affect their physicochemical properties and thus enhance their degradability.^{71,75,76} The integration of organic moieties, including S-S bonds, selenium-selenium (Se-Se) bonds, and amide bonds, within the framework of silica nanoparticles has paved the way for a highly controlled biodegradation pathway that can adapt to the specific conditions present in the tumor microenvironment. Influenced by specific enzymes, pH levels, and the unique redox environments inherent to tumor tissues, these bonds can rapidly undergo cleavage, leading to the release of therapeutic agents or imaging agents (Fig. 8).

2.2.1. S-S bond. Polysulfide linkages represent the predominant hybrid constituents encountered in degradable organosilica nanoparticles, predominantly encompassing two variations: disulfide bonds (S-S) and tetrasulfide bonds (S-S-S-S).^{26,54} The conventional preparatory approach involves the strategic utilization of alkyl groups to establish connections between sulfur bridges and central silicon atoms, subsequently followed by the condensation of the modified silica coupling agent with the siloxane network. Notably, polysulfide-hybridized silica nanoparticles exhibit a discernible responsiveness to degradation when exposed to an array of reducing agents, including glutathione (GSH),^{47,77-80} dithiothreitol (DTT),^{81,82} cysteine (Cys),⁸³ mercaptoethanol,^{84,85} and sodium borohydride.⁸⁶ The initial three compounds exemplify prototypical endogenous reducing agents. They frequently serve as benchmarks in investigations targeting the responsive release of therapeutics within the TME using hybrid silica-based drug delivery systems. It is widely acknowledged that

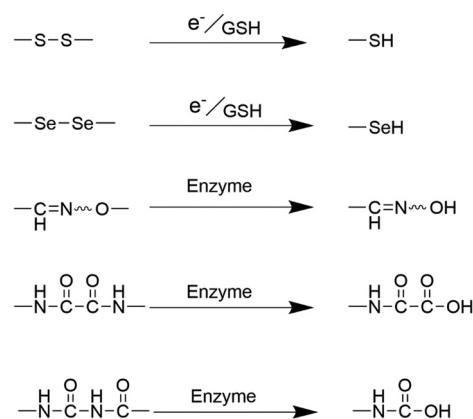


Fig. 8 Diagram illustrating the degradation mechanism of the organic moiety-doped silica nanoparticles.

the distribution of endogenous reducing agents such as GSH in the body is uneven. Notably, their intracellular concentrations substantially surpass those observed in extracellular tissue fluids, with a particularly elevated presence in tumor lesions. This distinctive concentration gradient within tumor sites engenders a noteworthy prospect for the development of targeted and responsive drug delivery systems that are strategically harnessed through the utilization of nanotechnology.

Dendritic mesoporous organosilica nanoparticles exhibit superior degradation performance compared to other silica nanoparticles due to their unique dendritic structure and pore design. The incorporation of disulfide or tetrasulfide bonds into these dendritic mesoporous organosilica nanoparticles enables the specific cleavage of sulfur–thiol bonds under specific conditions, facilitating nanoparticle degradation and enhancing their potential in drug delivery and other biological applications. Yang *et al.* reported the development of cancer cell-specific degradable dendritic mesoporous organosilica nanoparticles (DDMONs) (Fig. 9).⁷⁸ The nanoparticles possess well-distributed disulfide bonds within their controllable pores, enabling responsive degradation upon exposure to GSH. Serum incubation of the DDMONs demonstrated a partial structural collapse after 48 h in the presence of 1 mM GSH solution, while the spherical morphology remained largely unchanged. However, an elevated GSH concentration (10 mM) led to premature structural disruption of DDMONs. Furthermore, nanoparticle degradation was assessed by high-performance liquid chromatography (HPLC) and Ellman test across varying GSH concentrations. After 48 h of incubation of nanoparticles with a 1 mM GSH concentration, a modestly elevated oxidized GSH percentage (85%) was observed in DDMONs when compared to MONs (approximately 76%). Additionally, the OD value associated with the generated –SH content in DDMONs (0.20) was slightly greater than the value observed in MONs (0.17). However, at a higher GSH concentration of 10 mM, the percentage of oxidized

GSH in DDMONs decreased to approximately 32%, which was three times higher than that of MONs (11%). These results indicated that the porous structure of the DDMONs significantly influenced the degradation of the nanoparticles. To further investigate the cellular-level degradation of the nanomaterials, DDMONs-PEI were incubated in HEK293t normal cells and B16F0 melanoma cancer cells. TEM images unveiled rapid internalization and complete fragmentation of DDMONs-PEI within 4 h in B16F0 cells, whereas degradation was prominently inhibited in normal human cells due to lower GSH levels. Additionally, incubation of DDMONs-PEI with MCF-7 breast cancer cells, Chinese hamster ovary (CHO) normal cells, and RAW264.7 macrophages demonstrated significant degradation only in MCF-7 cancer cells. These findings highlighted the specific degradability of the nanoparticles towards cancer cells. Similarly, GSH-depleted dendritic mesoporous organosilica nanoparticles (GDMON) were ingeniously designed by incorporating embedded tetrasulfide bonds and featuring expansive dendritic mesopores. These nanoparticles demonstrated the capability to encapsulate ovalbumin (OVA) and unmethylated cytosine-phosphate-guanine (CpG).⁸⁷ Notably, the GDMON-P modified with PEI exhibited remarkable behaviour upon entering antigen-presenting cells (APCs) and experienced decomposition within the cytoplasm, primarily influenced by elevated concentrations of GSH. This process, in turn, triggers the release of antigens and adjuvants, thereby stimulating immune responses. Under the conditions of 2 mM GSH, both GDMON-P and NDMON-P (nonmacroporous) exhibited extremely gradual release of OVA, with only 4.2% and 5.3% of the antigen released after a span of 6 days, respectively. This sustained release profile was attributed to robust electrostatic and hydrophobic interactions between proteins and organosilica frameworks. Conversely, when exposed to 10 mM GSH, GDMON-P demonstrated a substantial enhancement in OVA release (19.8%) over the same 6-day period. In comparison, NDMON-P exhibited a slow release rate, with only 8.6% of the antigen released, which was attributed to GSH-triggered disruption of the pore structure. Further insights into the nanoparticle behavior after coincubation with APCs were gleaned through the utilization of bio-TEM. Within a mere 4 h time-frame, a substantial portion of the nanoparticles had undergone internalization by APCs. Following a 24 h incubation period, GDMON-P revealed partially collapsed structures, while the majority of the alkylated NDMON-P retained their intact architecture, providing valuable observations regarding the interplay between nanoparticles and cells.

Small silica nanoparticles exhibit substantial potential for various applications within the biomedical sector. They can function as highly effective platforms for drug delivery and therapeutic interventions, thereby contributing to the advancement of precision medicine and tailored treatment approaches. Notably, small-sized organosilica nanoparticles display significant degradation through the degradation of organic functional groups and dissolution of the silica framework. Yu *et al.* prepared ultrasmall disulfide-bridged organosilica nanoparticles (MONs) with diameters ranging from 15 nm to 45 nm.⁸⁸ Due to

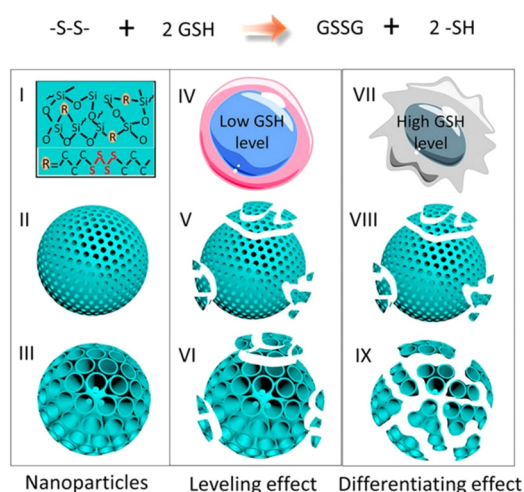


Fig. 9 An illustrative portrayal showcasing the structure and functional attributes of DDMONs. Reproduced from ref. 78 with permission from ACS, copyright 2016.

the incorporation of disulfide bonds within the framework of the MONs, a remarkably responsive behaviour to the intracellular GSH environment was exhibited. When placed in an SBF solution containing 10 mM GSH, the MONs underwent biodegradation over a span of 14 days, and subsequent TEM analysis did not reveal any intact spherical MONs. To delve further into the biodegradation dynamics at the cellular level, the MONs were cocultured with breast cancer 4T1 cells. Following a day of coculture, a substantial quantity of MONs was detected within the cytoplasm of the tumor cells. With prolonged incubation, a similar trend of structural collapse and nanoparticle dissolution behaviour emerged within a mere 2 days. On the third day of incubation, an even more pronounced biodegradation pattern was apparent, ultimately culminating in the observation of only a few collapsed MONs after 7 days of cultivation. Similarly, utilizing the “chemical homology” mechanism, Huang *et al.* ingeniously integrated disulfide bonds into the silica framework, resulting in the creation of scalable organic-inorganic hybrid hollow mesoporous organosilica nanoparticles (HMONs) (Fig. 10).⁸⁰ The HMONs exhibit appreciable degradability due to the presence of disulfide bonds. The dynamic changes in the microstructural evolution of HMONs in SBF were meticulously examined using TEM. During the initial 7-day period, no significant structural alterations were evident; however, on the 11th day, there was a notable proliferation of structural collapses. Notably, in an SBF solution containing GSH (10 mM), the degradation rate of the HMONs was significantly accelerated, culminating in an almost complete absence of intact spherical HMONs after 14 days. Furthermore, upon uptake by 4T1 cells, a similar trend of structural collapse and dissolution was observed within a mere 2 days, with only a limited number of nanostructured, collapsed HMONs remaining discernible after 7 days. To significantly improve the precision, effectiveness, and safety of cancer therapy, developing a therapeutic that is finely tuned to the TME could achieve enhanced therapeutic outcomes. Building upon this concept, Lu *et al.* innovatively engineered thioether-

bridged organosilica nanoparticles (DOX-CuS@PMOs) *via* the sol-gel method. The intricate design aimed to synergistically enhance CMT through photothermal effects, capitalizing on a triple response mechanism involving GSH, pH variations, and laser irradiation.⁴⁵ The CuS@PMOs possessed disulfide bonds that render them degradable in GSH solution. Under conditions of pH 7.4 and 10 mM GSH, DOX-CuS@PMOs exhibited controlled degradation, releasing 20% of DOX within just 1 h and surpassing 40% within 8 h. In the absence of GSH, the release of DOX from DOX-CuS@PMOs was limited to only 13% over 8 h. Moreover, when simulating the conditions of intracellular endosomes/lysosomes (pH 5.5, 10 mM GSH), the nanomaterials showed an accelerated cumulative release amount of 62.5% after 8 h.

2.2.2. Se-Se bond. Selenium-selenium (Se-Se) bonds have gained significant attention in recent years due to their unique properties and potential applications in various fields. Researchers have discovered that Se-Se bonds can enable pH-responsive, redox-responsive, and tumor-specific enzyme-catalyzed cleavage. Therefore, the integration of Se-Se bonds into the silica framework has the capacity to broaden the application prospects of silica nanoparticles within the realm of biomedicine. Shao *et al.* developed a synthesis method utilizing bis[3-(triethoxysilyl)propyl]diselenide (BTESePD) as a selenide source, leading to the creation of diselenide bond-bridged MONs with a notably high selenium content (9.9%). This innovation aimed to facilitate accelerated biodegradation through an X-ray- and ROS-responsive mechanism (Fig. 11a).⁸⁹ In a solution containing 100×10^{-6} M H_2O_2 , mimicking ROS conditions in the TME, the organosilica frameworks underwent structural collapse, forming irregular aggregates within 24 h and complete decomposition within 3 days upon exposure to low-dose X-ray radiation (1 Gy) (Fig. 11b). It is noteworthy that while the MONs exhibited degradation upon X-ray irradiation, they did not undergo further decomposition in the absence of H_2O_2 . The transformation into selenic acid was verified through an elevation in the binding energy of Se3d5 from 56 to 60 eV, as observed by X-ray photoelectron spectroscopy (XPS) (Fig. 11c). This shift suggests that Se-Se bonds can be oxidized and cleaved in the presence of X-rays and ROS, highlighting a key mechanism underlying the process.

2.2.3. Amide bond. Amino acids are ubiquitous molecules found within living organisms. Incorporating amino acids can confer a distinct level of bioreactivity on silica nanoparticles, enabling them to undergo modifications in specific biological contexts, such as enzymatic degradation. This attribute facilitates precise control over drug release mechanisms. Ratirotjanakul *et al.* utilized a copolymerization approach between TEOS and amino acids (aâs), *i.e.*, glycine, aspartic acid, and cysteine, which were conjugated with 3-isocyanatopropyltriethoxysilane (aâ-ICPTES), to synthesize mesoporous silica nanoparticles (aâ-MSNs).⁹⁰ Analysis through microwave plasma atomic emission spectroscopy (MP-AES) revealed that the %Si dissolution rate of aâ-MSNs in PBS/pancreatin enzyme solution at pH 7.4 was 3–5 times higher compared to that in PBS and 7–8 times higher compared to that in acetic acid buffer solution (pH 5.2). Among

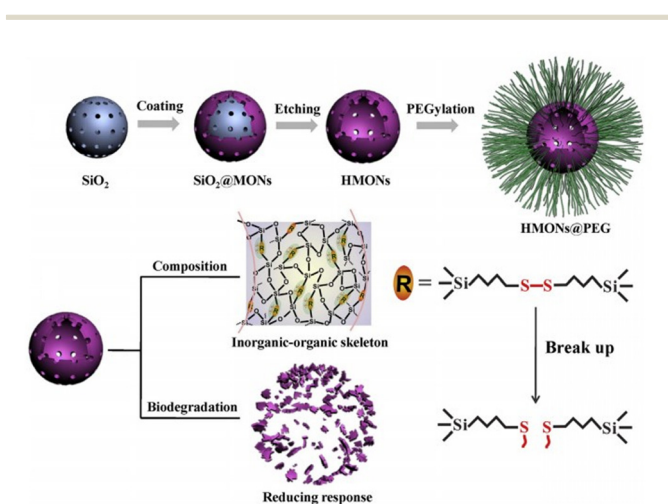


Fig. 10 Synthesis and degradation of HMONs. Reproduced from ref. 80 with permission from Elsevier, copyright 2017.

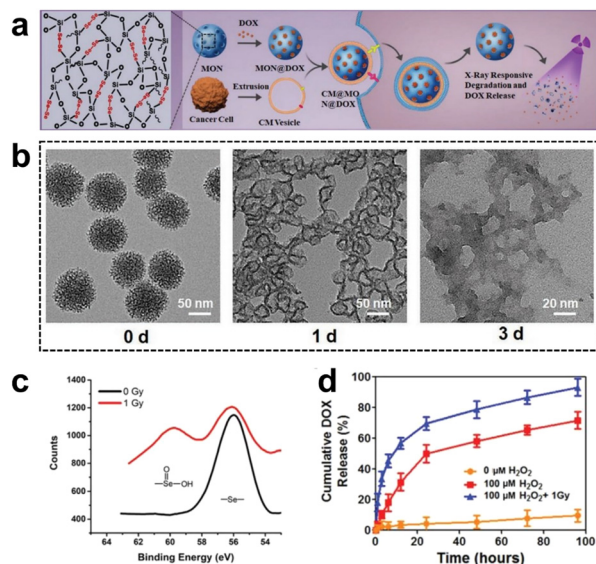


Fig. 11 (a) Synthesis and application of selenium-containing organosilica nanoparticles. (b) TEM images of SeMONs subjected to 1 Gy X-ray radiation in the presence of H₂O₂. (c) XPS analysis of SeMONs before and after radiation. (d) Drug release experiments of SeMONs. Reproduced from ref. 89 with permission from Wiley, copyright 2020.

the three culture media, aspartic acid-MSNs with two carboxyl groups exhibited the highest degradation, followed by cysteine-MSNs and glycine-MSNs. In addition, Zhang *et al.* selected histidine to prepare histidine bis(oxalate)silane (His-BOP), which served as an organosilica precursor. His-BOP was then cocondensed with TEOS in the presence of the P123 template to fabricate histidine-containing periodic mesoporous organosilica (His-PMO) under acidic conditions (Fig. 12).⁹¹ Capitalizing on the abundant functional groups of histidine and the distinctive mesoporous channels of PMO, His-PMO exhibited robust electrostatic interactions with drugs and displayed a notable drug loading capacity of up to 28 mg g⁻¹. *In vitro* drug release investigations were conducted using various pH culture media. The findings indicated an escalated cumulative release amount and variable nonlinear release kinetics of paclitaxel (PTX) with decreasing pH (5.2, 6.8, and 7.4) over time.

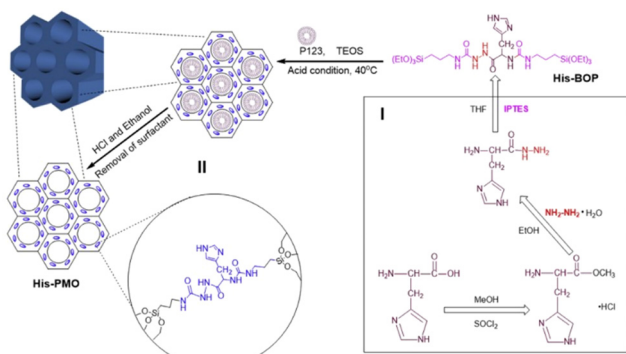


Fig. 12 Schematic diagram of the synthesis of His-PMO. Reproduced from ref. 91 with permission from Elsevier, copyright 2019.

Oxamide, an organic compound encompassing an amino group and an acylamide group, serves as a reactive small molecule akin to amino acids. Fatiev *et al.* devised a bridged bis-siloxane (BS) nanoplat-form with an organic content of approximately 50%. This was achieved by employing oxamide as a bridging agent *via* a sol-gel reaction mediated by alkoxy-silane precursors (Fig. 13a).⁹² Subsequently, they investigated the biodegradation performance of the BS nanoparticles in simulated biological media. The nanoparticle suspensions were exposed to Tris buffer (pH 4), PBS buffer (pH 7.4), and PBS/pancreatin solution. Experimental findings demonstrated that pancreatin could cleave amino acids into carboxylate and ammonium ion groups, consequently triggering BS nanoparticle degradation solely in the presence of pancreatin. Dynamic light scattering (DLS) measurements exhibited a reduction in particle size after 24 h and 48 h, with an initial mean hydrodynamic diameter of 295 nm dwindling to 122 nm after 48 h of incubation in PBS/pancreatin.

Cystamine consists of two amino groups connected by a sulfur atom and is known to possess various physiological and pharmacological activities in biological systems. The thiol group (–SH) in cystamine can react with the silane groups on the oxidized silica reactants to form cystamine disulfide, which imparts the characteristics of organic–inorganic redox-responsive degradation. Based on this, Kummara *et al.* adopted a cocondensation method to introduce cystamine-modified organosilane functionalities into the POM framework, leading to the creation of Cys-PMO hybrid nanoparticles for loading DOX to combat human cervical cancer (Fig. 13b).⁹³ Notably, this system incorporated disulfide linkages (–S–S–) alongside additional carboxylic acid moieties. As a result, Cys-PMO hybrid nanoparticles manifested a robust drug loading capacity and exhibited pH- and redox-responsive attributes. The outcomes of *in vitro* release experiments revealed that following 48 h of incubation in PBS (pH 7.4), pH 5.5, and pH 5.5/10 mM DTT solution, the percentages of DOX released from Cys-PMO hybrid nanoparticles were 10%, 56%, and 89%, respectively.

2.2.4. Methylene blue. To address the challenge of achieving both controlled release and self-destruction of very small fragments of the carrier, Zhang and colleagues developed a novel approach to create SiO₂–drug composite nanoparticles.⁹⁴ This was achieved by incorporating drug molecules into the

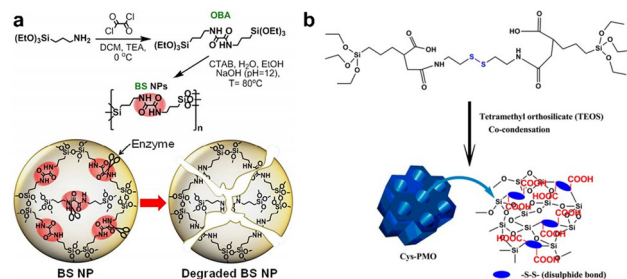


Fig. 13 (a) Illustrative depiction of the synthesis and enzyme-triggered degradation process of BS nanoparticles. Reproduced from ref. 92 with permission from The Royal Society of Chemistry, copyright 2015. (b) Schematic outlining the preparation of Cys-PMO hybrid nanoparticles. Reproduced from ref. 93 with permission from ACS, copyright 2018.

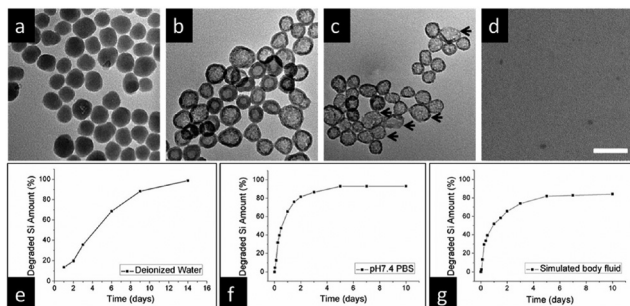


Fig. 14 (a) Representative TEM images of SiO₂-MB nanoparticles following immersion in deionized water for varying durations: (a) 1 day, (b) 4 days, (c) 9 days, and (d) 14 days. Scale bar, 100 nm. Quantitative analysis using ICP-OES reveals the degradation of silicon content as a function of immersion time across distinct environments: (e) deionized water at room temperature, (f) PBS (pH 7.4), and (g) simulated body fluid (containing 50% FBS) at 37 °C. Reproduced from ref. 94 with permission from ACS, copyright 2013.

silica matrix during the growth process of the nanoparticles. Taking methylene blue (MB) as an example, it is demonstrated that a radial concentration gradient of MB was established within the nanoparticles, leading to the simultaneous occurrence of MB release and SiO₂ carrier decomposition, driven by the diffusion of drug molecules. Interestingly, the onset of this decomposition process was triggered by the gradual diffusion of MB molecules from the carrier matrix. This process of degradation was observed to commence from the central region of the nanoparticles, as inferred from the time-dependent morphological changes observed when the nanoparticles were dispersed in an MB-soluble solvent. This discernible trend could be attributed to the concentration disparity, with the central region of the nanoparticles predominantly housing a higher concentration of MB molecules and relatively limited incorporation of SiO₂. Consequently, the “bone” structure of the carrier was rendered particularly vulnerable in this central zone. As the MB molecules continued to diffuse out of the nanoparticles, the cohesive SiO₂ “network” (which underwent concurrent development with MB during nanoparticle formation) experienced deterioration, ultimately culminating in the complete disintegration of the nanoparticles upon the release of all drug molecules (Fig. 14). Of particular interest is the interdependence observed between the rate of MB release and the decay of the SiO₂ carrier, contingent upon the concentration of MB within the source material during nanoparticle growth. Once the loaded drug was completely released, the self-decomposable SiO₂ nanocarrier underwent fragmentation into smaller fragments. This fragmentation allowed for easy excretion from the body through the renal system.

3. TME-triggered degradable silica nanoparticles for precision cancer theranostics

Within the confines of the TME, the interplay of tumor cell growth, metabolism, and intricate interactions with adjacent

cellular and molecular components culminate in the emergence of distinctive biological and physiological attributes.^{95,96} These include an acidic environment, heightened redox status, elevated concentrations of specific biomolecules (*e.g.*, growth factors, enzymes, *etc.*), and varying expression of cell types and surface receptors.^{9–13,97} TME-responsive nanotherapeutics are diagnostic and therapeutic agents specifically engineered to target the TME in cancer and are capable of responding to specific conditions or signals within the TME, thereby achieving precise diagnosis and treatment.^{13,98} These nanotherapeutics hold significant promise in the realms of cancer theranostics, as they have the potential to enhance treatment effectiveness, minimize side effects, and propel the advancement of personalized medicine. In this section, we systematically present the latest advancements in the research of TME-responsive degradable silica nanoparticles, elucidating representative types of biological triggers, including pH, redox, hypoxia, and enzymes.

3.1. Single biological triggers

3.1.1. pH. Tumors, due to their faster glycolytic metabolism, often generate significant amounts of lactate and hydrogen ions (H⁺). This accumulation of H⁺ leads to lower pH values both inside and outside tumor cells, with the extracellular pH ranging from 6.4 to 6.8 and the intracellular pH ranging from 4.5 to 5.5, in contrast to normal tissues, where the extracellular pH is 7.4 and the intracellular pH ranges from 5.0 to 6.0.^{99,100} This acidic TME not only accelerates tumor progression and metastasis but also contributes to treatment failure.¹⁰¹ Recently, the pH-responsive property of degradable silica nanoparticles has allowed them to achieve precise release of active substances, such as imaging agents, in acidic environments, thus improving the diagnostic and therapeutic effects.^{44,102,103} These platforms mainly involve two strategies: one involves pH-responsive chemical bond cleavage, where chemical bonds remain stable at neutral pH but break in weakly acidic conditions, such as hydrazone bonds and imine bonds.¹⁰⁴ The other strategy is pH-responsive charge reversal, which occurs when the surfaces of specific polymers undergo a change in charge in response to pH variation in the TME, enabling targeted responses.¹⁰⁵ pH-responsive degradable silica nanoparticles are usually designed to undergo morphological or structural changes in the acidic TME, thereby achieving accurate localization and specific cancer diagnosis and treatment. Li *et al.*¹⁰⁶ developed a novel theranostic platform (MP@MS) by utilizing a biodegradable magnetic silica-sealed mesoporous polymer. By incorporating biodegradable materials and utilizing a silica-sealing strategy, nanocomposites can achieve precise drug delivery, controlled drug release, and enhanced imaging capabilities. Under the acidic TME, the ultrathin nanoshells were selectively biodegraded, triggering sustained and controlled drug release. Furthermore, iron doping endowed the platform with magnetic targeting and magnetic resonance (MR) imaging capabilities in the tumor. This innovative approach has the potential to significantly improve the safety and efficacy of cancer theranostics, offering a promising strategy for

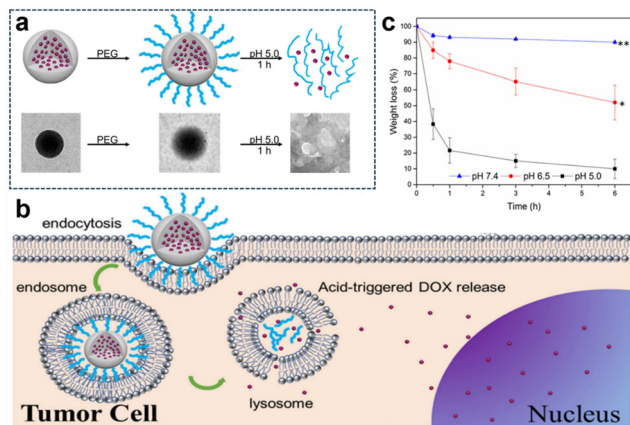


Fig. 15 (a) Schematic representation and TEM images of the preparation and degradation of DOX@OSNP-PEG₁₀₀₀. (b) Drug loading and release from biodegradable DOX@OSNP-PEG₁₀₀₀. (c) *In vitro* degradation of DOX@OSNP-PEG₁₀₀₀ at different pH values. Reproduced from ref. 107 with permission from Elsevier, copyright 2020.

personalized and targeted cancer treatment while minimizing side effects.

In the acidic TME, pH-responsive nanoplatforms can release drugs and achieve targeted therapy for tumor cells. This targeted drug delivery approach enhances drug accumulation in tumor tissues, improving treatment effectiveness while minimizing damage to healthy tissues. Peng *et al.*¹⁰⁷ synthesized rapidly biodegradable nanovectors (DOX@OSNP-PEG₁₀₀₀) by loading DOX into organosilica nanoparticles (OSNPs) and subsequently coating them with poly(ethylene glycol) (PEG) (Fig. 15a and b). The presence of the phenyl group and pH-sensitive imine bonding in the OSNPs facilitated DOX loading through hydrophobic interactions and triggered drug release in response to the acidic environment. *In vitro* degradation experiments revealed that the weight loss of the nanocarriers was only 10% within 6 h under physiological conditions of pH 7.4, whereas it reached 49% under acidic conditions (pH 6.5). Notably, under simulated lysosomal acidic environmental conditions (pH 5.0), the weight loss of OSNPs was 62% within half an hour and further increased to 90% within 6 h (Fig. 15c). This demonstrated the rapid biodegradability of the OSNPs, particularly in acidic environments, which made them highly suitable for endosomal-triggered drug delivery. Similarly, Zhang *et al.*⁹¹ prepared a histidine periodic mesoporous organosilica nanosystem (His-PMO) for sustained drug release. Since the imidazole moiety of histidine is prone to protonation under acidic conditions, leading to its electrostatic repulsion with drugs, it endowed His-PMO with excellent pH-responsive drug release behavior. To enhance targeted drug delivery, Kang *et al.*⁶⁹ developed a multifunctional target nanoplatform (oHA-DOX@MSNs/HAP) coated with oligo hyaluronan (oHA) and containing silica and HAP for targeted cancer treatment. By introducing oHA on the surface of the nanoplatform, oHA-DOX@MSNs/HAP could selectively bind to tumor cells, enabling precise recognition and targeted therapy for tumor cells. Moreover, silica and HAP underwent gradual degradation

under weakly acidic conditions and were cleared by metabolism. After exerting their effects on the body, they gradually degrade and release drugs, enabling precise targeted tumor therapy while avoiding adverse effects on healthy tissues.

By capitalizing on the unique conditions within tumors, therapeutic agents are activated precisely where needed, optimizing treatment efficacy. Furthermore, the inclusion of external stimuli, such as light or magnetic fields, adds an additional layer of control, allowing for on-demand drug release. Wu *et al.*¹⁰⁸ developed a highly versatile platform that synergistically combined targeted chemo-PTT. This was achieved through the utilization of thioether-bridged mesoporous organosilica nanoparticles (PMOs) as carriers for loading DOX. To facilitate precise targeting, bovine serum albumin-FA-modified MoS₂ sheets (MoS₂-PEI-BSA-FA) were synthesized and acted as effective capping agents for PMOs (Fig. 16a). Upon cellular uptake through FA receptor-mediated endocytosis, the nanoparticles were successfully encapsulated within endosomes. Under 808 nm laser irradiation, the DOX encapsulated in this nanocomplex exhibited a dual-stimuli responsive release, particularly in the acidic TME, thereby promoting targeted CMT. Additionally, the nanoplatform showed efficient conversion of NIR light energy into thermal energy, thereby enabling photothermal therapy. Furthermore, the release of DOX was expedited in the acidic environment (pH 5.0) compared to pH 7.4, with the maximum cumulative release amount observed at pH 5.0, especially when combined with 808 nm laser irradiation (Fig. 16b). This pH-dependent and NIR-stimulated release of DOX significantly enhanced the synergistic effect of chemophotothermal therapies, underscoring the enormous potential of this nanoplatform as a highly promising approach for effective cancer treatment.

3.1.2. Redox. The concentration of GSH is significantly elevated due to the enhanced metabolic activity resulting from the rapid cancer cell growth and proliferation.⁵ GSH exhibits a substantial concentration difference (100–1000 times) between intracellular ($2\text{--}10 \times 10^{-3}$ M) and extracellular ($2\text{--}20 \times 10^{-6}$ M) environments.^{76,109} The elevated levels of GSH in tumors highlight its importance as a target for therapeutic interventions. By

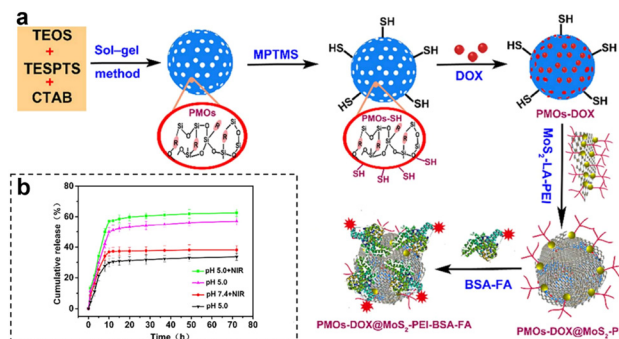


Fig. 16 (a) Schematic synthesis and preparation of PMOs-DOX@MoS₂-LA-PEI-BSA-FA composites. (b) DOX release profiles of PMOs-DOX@MoS₂-PEI-BSA-FA nanocomposites at different pH values, with and without NIR laser irradiation (808 nm, 1 W cm⁻²). Reproduced from ref. 108 with permission from Elsevier, copyright 2018.

incorporating metal ions (e.g., Mn^{2+}) or organic moieties (e.g., disulfide bonds) into silica nanoparticles, they can selectively breakdown in high GSH environments.^{46,76,84,85,110} When the degradable silica nanoparticles enter the tumor tissue, GSH reacts with these nanomaterials, leading to specific chemical changes in their structure or morphology.⁸⁸ These GSH-responsive changes can be monitored using imaging techniques or other detection methods, enabling precise localization of the tumor tissue. Additionally, these degradable silica nanoparticles can also carry drugs or imaging agents and achieve precise release under GSH-responsive conditions, thereby enhancing therapeutic or imaging effects.⁸⁴ Moreover, the breakdown of these nanomaterials aids in their metabolism and excretion, thus ensuring excellent biocompatibility.

In the field of MR imaging, manganese ions could serve as contrast agents to enhance the visibility of MR images. However, in practical applications, MnO_2 is often found in the nanoparticle form. In this state, it is less suitable for direct use as an MR imaging contrast agent due to its limited ability to produce a strong MR imaging signal. This is where GSH plays a pivotal role. GSH can initiate a chemical reaction with MnO_2 , converting it into soluble Mn^{2+} . These Mn^{2+} ions can then be sequestered within the body or specific biological tissues, subsequently facilitating their utilization for MR imaging. Zheng *et al.*¹¹¹ synthesized a TME-responsive nanotheranostic agent (FMSN- MnO_2 -BCQ) that integrated precise MR imaging and NIR-II fluorescence imaging with self-reinforcing antitumor therapy (Fig. 17). The core component of this nanotheranostic platform was thioether-doped organosilica. GSH prompted the degradation of FMSN- MnO_2 -BCQ within the TME, effectively releasing BCQ and MnO_2 , with their ultrasmall size facilitating tumor penetration. One of the key features of this nanotheranostic platform was its ability to offer precise and high-resolution imaging capabilities. The real-time imaging capabilities provided by MR imaging and NIR-II fluorescence imaging enable precise tumor targeting, ensuring

efficient drug delivery and enhancing treatment efficacy. This aspect is crucial for early detection and effective monitoring of treatment response, providing valuable insights for personalized cancer therapy. Moreover, the nanoparticles are engineered to carry therapeutic agents and photothermal agents within their silica framework. When exposed to NIR-II laser irradiation, photothermal agents generate localized heat, triggering drug release and enhancing the therapeutic effect on cancer cells. Furthermore, in the presence of GSH, MnO_2 is reduced to Mn^{2+} , acting as a Fenton reagent that converts endogenous H_2O_2 into highly cytotoxic $\cdot\text{OH}$, enabling selective chemodynamic therapy (CDT). Additionally, the continuous depletion of endogenous GSH weakens the capacity to clear free radicals, leading to a self-enhancing effect of the CDT.

Similarly, Wei *et al.*¹¹² designed a virus-like mesoporous silica nanoprobe (VGd@ICG-FA) capable of achieving NIR-II fluorescence imaging and inducing ferroptosis by RT sensitization. The nanoprobe was obtained by utilizing tetrasulfide-bridged silica nanoparticles to load the photosensitizer ICG, which was then coated with gadolinium (Gd) and anchored with FA. VGd@ICG-FA exhibited efficient targeting of tumor cells facilitated by its virus-like morphology and FA anchoring. This nanoprobe was particularly effective at identifying small cancers and guiding precise surgery using NIR-II fluorescence imaging. Once inside the cancer cell cytoplasm, the tetrasulfide linkages in the silica framework were disrupted by GSH. Consequently, the framework exhausted GSH, leading to the disruption of intracellular reactive ROS homeostasis. Additionally, Gd generated more ROS during RT, further triggering ferroptosis and enhancing the effectiveness of RT in breast cancer treatment. Quantitative analysis of fluorescence intensity revealed that VGd@ICG-FA exhibited a fluorescence signal 7.59 times stronger within mammary tumors compared to normal tissues. This substantial contrast was sufficient for the effective differentiation between tumors and normal mammary tissue. Following intravenous administration of VGd@ICG-FA for 36 h, five pairs of mammary tumors were surgically removed in segments under NIR-II fluorescence imaging. The fluorescence intensity of the excised tumors was notably higher than that of the surrounding muscle tissue, yielding a tumor-to-muscle (T/M) ratio of 8.01 ± 0.62 . In addition, Guo *et al.*¹¹³ developed a biodegradable nanoplatform (HMON@CuS/Gd) that incorporated Cu nanocrystals and Gd-doped hollow mesoporous organosilica nanotheranostics (HMON) (Fig. 18a). This nanoplatform offered multimode imaging and PTT capabilities. In the TME with elevated GSH concentration, the disulfide bonds within the HMON framework responded to GSH, leading to nanoplatform degradation and subsequent release of CuS and Gd^{3+} . When exposed to NIR light, CuS underwent photothermal conversion, inducing ROS generation and compromising mitochondrial function in tumor cells, resulting in effective photothermal therapeutic effects. Additionally, Gd^{3+} acted as a radiation sensitizer, enhancing X-ray photon capture and improving MR imaging efficacy. Moreover, the nanoplatform could encapsulate the carbon cyanine dye DIR, enabling NIR fluorescence imaging

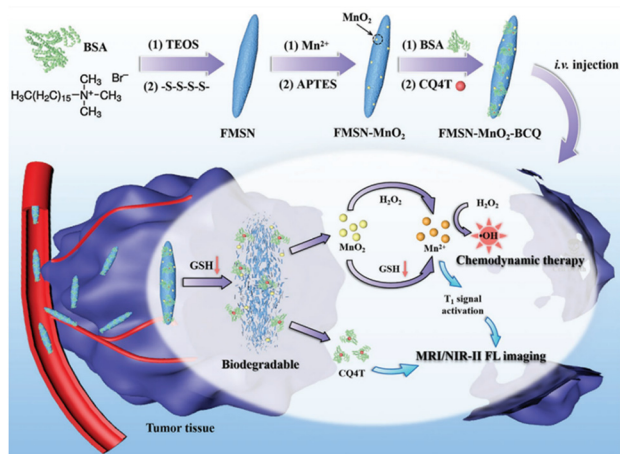


Fig. 17 Diagram of the synthesis process of FMSN- MnO_2 -BCQ and the mechanisms for MR imaging, NIR-II fluorescence imaging and enhanced CDT. Reproduced from ref. 111 with permission from Wiley, copyright 2021.

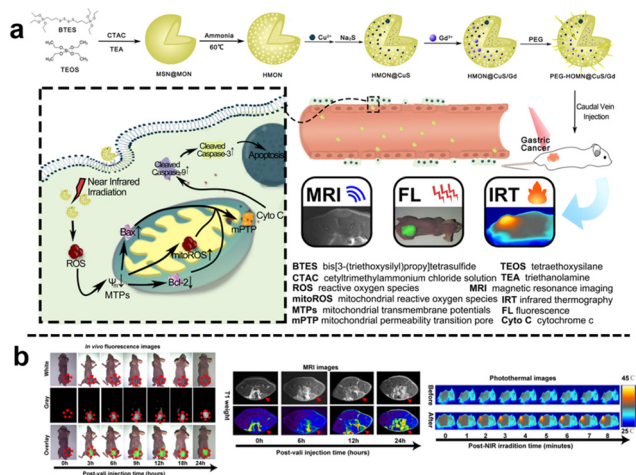


Fig. 18 (a) Schematic diagram of the synthesis and mechanism of anti-tumour action of HMON@CuS/Gd. (b) *In vivo* FL/MIR/IRT images of HMON@CuS/Gd. Reproduced from ref. 113 with permission from Springer Nature, copyright 2020.

and facilitating image-guided visualization. Experimental results demonstrated the nanoplatform's effectiveness in accumulating fluorescence signals, significantly enhancing T_1 -weighted MR imaging signals for improved MR imaging, and substantially inhibiting tumor growth (Fig. 18b).

CDT is an innovative therapeutic strategy that employs catalytic reactions to produce ROS from either internal or external sources. This, in turn, triggers oxidative stress within cells, ultimately resulting in cell death. Despite its potential, CDT faces hurdles in fully realizing its benefits, primarily stemming from difficulties in achieving accurate tumor targeting and efficiently disrupting cellular redox homeostasis. To address these issues, Lu *et al.*¹¹⁴ engineered specialized nanoparticles (nanoMIPs) that could target tumor tissues and disrupt cellular redox homeostasis, which were initially prepared as biodegradable silica nanoparticles loaded with Cu^{2+} and subsequently subjected to *in situ* functionalization using Tn antigen (GalNAc) as a template through molecular imprinting technology. The nanoMIP was specifically designed to selectively target tumor cells that overexpressed the Tn antigen, thereby facilitating enhanced cellular uptake. Upon internalization by tumor cells, the nanoMIPs underwent controlled degradation in response to the TME. This degradation process led to the spontaneous release of $\text{Cu}^{2+}/\text{Cu}^+$ through redox cycles, resulting in highly potent depletion of GSH and triggering $\cdot\text{OH}$ generation through a Fenton-like reaction. The produced Cu^+ could effectively inhibit catalase activity, thereby indirectly elevating the endogenous H_2O_2 level within the tumor cells. Consequently, the “maladjusted” tumor cells lost their resistance against $\cdot\text{OH}$ -induced damage, ultimately culminating in tumor cell apoptosis. By interfering with cellular redox processes, the nanoparticles sensitized tumor cells to oxidative stress, making them more susceptible to CDT effects. Both *in vitro* and *in vivo* experiments unequivocally demonstrated the exceptional cytotoxicity of nanoMIPs against tumor

cells and their remarkable efficacy in inhibiting tumor growth in a xenograft tumor model while simultaneously exhibiting minimal side effects.

Immunotherapy utilizes the body's immune system to precisely target and eliminate cancer cells, potentially achieving long-lasting remission or even a cure. It typically causes fewer side effects than traditional treatments such as CMT, enhancing patient well-being. Incorporating Se–Se moieties into the silica framework not only enables precise control of the degradation rate of silica nanoparticles but also confers GSH responsiveness to them. Zhang *et al.*¹¹⁵ developed a coordination and redox-responsive nanoplatform (MON@KP1339) for chemoimmunotherapy by utilizing diselenide-bridge mesoporous organosilica nanoparticles (MONs) to load the ruthenium compound KP1339 (Fig. 19a). The incorporation of GSH-responsive diselenide bridges enabled the nanoplatform to achieve controlled degradation, thereby effectively regulating the release of KP1339. KP1339 could promote immunogenic cell death (ICD) in tumor cells, leading to increased antigen release and stimulation of the host immune system's response, consequently bolstering the therapeutic efficacy and ultimately achieving the goal of chemoimmunotherapy. Moreover, the cumulative release amount of KP1339 from MON@KP1339 exceeded 70% after 12 h under simulated tumor cell GSH conditions, whereas the control group without GSH exhibited a cumulative release amount of less than 10% within 96 h (Fig. 19b). This result clearly indicated that the GSH-responsive environment facilitated the controlled release of KP1339. *In vivo* experiments further demonstrated remarkable tumor growth inhibition by MON@KP1339, indicating outstanding antitumour efficacy

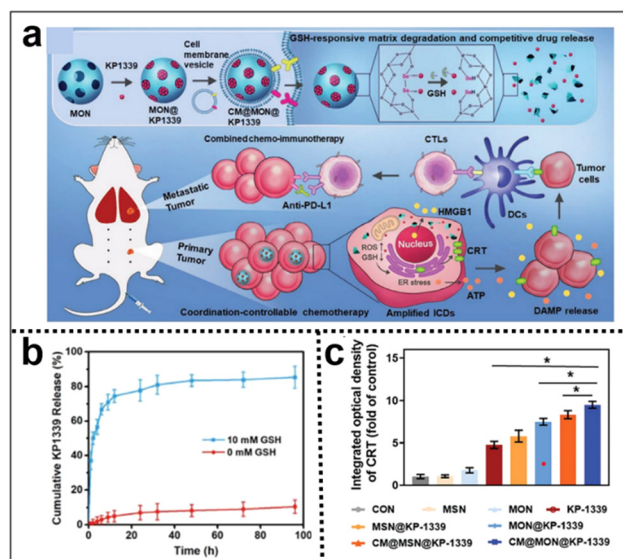


Fig. 19 (a) Illustration of the synthesis of diselenide-bridged MONs for responsive drug release and enhanced ICD to facilitate effective and safe cancer chemoimmunotherapy. (b) The cumulative release profiles of KP1339 cells in the presence or absence of GSH. (c) Semiquantitative analysis of the primary tumor's exposure to CRT in each experimental group. Reproduced from ref. 115 with permission from Wiley, copyright 2021.

(Fig. 19c). In another study, Li *et al.*¹¹⁶ constructed an *in situ* therapeutic nanovaccine (HMSsN-ANX5@HOMV) by utilizing diselenide-bridged hollow mesoporous organosilica nanoparticles (HMSsN) to load Annexin A5 (ANX5). These nanoparticles were subsequently enclosed within bacterial outer membrane vesicles (OMVs) and surface-modified with HA. The incorporation of diselenide bridges for ANX5 immobilization not only retained the protein's biological activity but also facilitated the TME-responsive release of ANX5. Upon accumulation within the TME, HMSsN-ANX5@HOMV was exposed to elevated levels of GSH, triggering the cleavage of diselenide bridges and facilitating the rapid release of encapsulated annexin A5 protein. Annexin A5 plays a pivotal role in tumor cell apoptosis by selectively binding to phosphatidylserine on the surface of apoptotic cells, effectively impeding their phagocytosis by macrophages and subsequently enhancing the response of cytotoxic T cells, a crucial subset of immune cells responsible for tumor cell recognition and elimination, thereby eliciting robust antitumor effects. By augmenting the activity of cytotoxic T cells, the liberated annexin A5 protein effectively promoted antibody-dependent cellular cytotoxicity and targeted immune responses against the tumor, ultimately restraining tumor growth and metastasis. The *in vivo* results of the *in situ* therapeutic vaccine demonstrated the complete eradication of approximately 50% of 4T1 tumors and induced long-term immune memory.

The integration of diverse therapies in cancer treatment provides several benefits. Synergistic effects can boost treatment efficacy, potentially improving tumor control and response rates. This approach overcomes individual treatment limitations, such as drug resistance or incomplete tumor elimination. In a breaking study by Liu *et al.*,¹¹⁷ a novel nanocomposite (DCC-HA NCs) was developed that exhibited rapid responsiveness in the TME (Fig. 20a and b). This remarkable nanocomposite comprised tetrasulfide bond-incorporated dendritic mesoporous organosilica (DMOS) as a highly efficient nanocarrier coupled with a newly engineered hydrogen sulfide (H_2S) gas generator. Additionally, it was ingeniously loaded with chloroperoxidase (CPO) and CaO_2 -HA, thus enabling the concurrent application of H_2S gas therapy, trimodal-enhanced enzyme dynamic therapy (EDT), and Ca^{2+} -interference therapy. The hallmark feature of this nanocomposite is its dynamic adaptability to the intricate microenvironment of the tumor. Upon entry into the tumor region, the nanocomposite experienced swift decomposition, attributed to the presence of tetrasulfide bonds, culminating in the controlled release of therapeutic H_2S gas. Moreover, the strategically incorporated CPO and CaO_2 -HA synergistically enhanced the efficacy of EDT and Ca^{2+} interference therapy, respectively, thereby offering a comprehensive and potent treatment strategy. CDT holds great promise as a therapeutic strategy, leveraging ROS generated *via* Fenton or Fenton-like reactions to induce oxidative stress and trigger tumor cell death.

3.1.3. Hypoxia. Cancer cells exhibit remarkably high proliferative activity, leading to their growth rate being typically faster than that of surrounding normal tissues. The tumor's

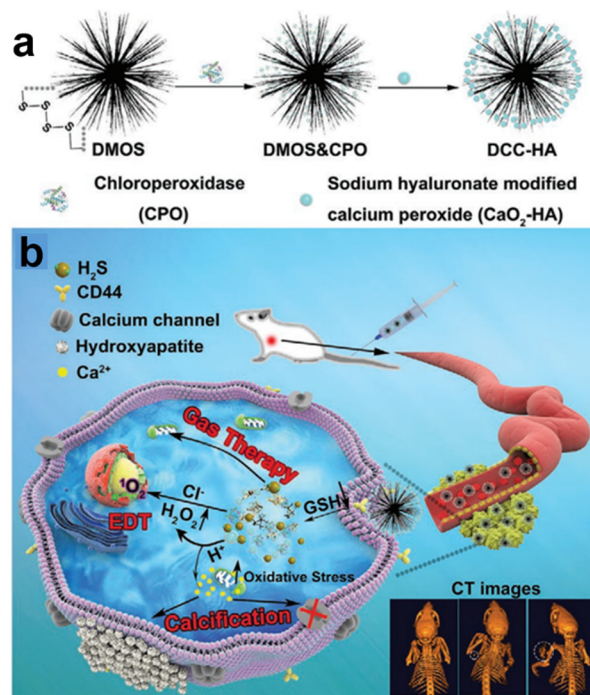


Fig. 20 (a) and (b) Schematic diagram of DCC-HA NCs for gas therapy and enzyme dynamic therapy (EDT). Reproduced from ref. 117 with permission from Wiley, copyright 2021.

internal vascular system faces a challenge in meeting the rapid demands for cell proliferation due to insufficient blood supply. Consequently, tumor tissues often develop abnormal vascular networks, causing stasis and reduced blood flow, which in turn leads to tumor hypoxia.^{118–121} Under conditions of inadequate oxygen supply, the effectiveness of tumor treatments, including CMT, RT, and phototherapy, is limited, resulting in severe consequences such as tumor recurrence and high mortality rates.^{118,122,123} Notably, quinones, nitroaromatics, azobenzene derivatives, and other functional groups serve as examples of hypoxia-responsive moieties.^{124,125} Researchers have made significant progress by developing hypoxia-responsive nanotheranostic systems based on degradable silica nanoparticles, offering new insights into cancer theranostics.⁶ The self-cleavage ability of these moieties under hypoxic conditions has facilitated the development of numerous optical probes, with azobenzene linkers being particularly common in the design of hypoxia-responsive carriers.¹²⁶

Hypoxia-responsive fluorescence imaging allows for the specific visualization of regions within tumors that are experiencing low oxygen levels. Gaining insights into the extent of tumor hypoxia can aid medical professionals in anticipating patient responses to these treatments and making necessary adjustments to treatment strategies. This selective targeting enhances the accuracy of disease detection and assessment. Yang *et al.*¹²⁷ prepared a nanosensor (HMON-Ce6-[[Ru(dpp)₃]]Cl₂) for real-time oxygen monitoring during photodynamic therapy (PDT) by synthesizing thioether-bridged deformable hollow mesoporous organosilica

nanoparticles and loading an oxygen-sensitive probe $[(Ru(dpp)_3)Cl_2]$ and a photosensitizer chlorin e6 (Ce6). As the irradiation time of HMON-Ce6- $[(Ru(dpp)_3)Cl_2]$ in the PDT increased, oxygen was transformed into ROS by Ce6. Following excitation at 463 nm, there was a linear increase in fluorescence emission at 620 nm, which correlated with the declining oxygen concentration. This observation demonstrates the nanosensor's sensitive response to changes in oxygen concentration. When HMON- $[(Ru(dpp)_3)Cl_2]$ was injected intratumorally into T98G-loaded mice, the nanosensor showed weak red fluorescence before 660 nm laser irradiation, but the fluorescence signal was significantly increased after laser irradiation. The corresponding radiation efficiency of the tumor was significantly increased, which could respond to oxygen consumption in the process of PDT. Similarly, Yuan *et al.*⁸¹ developed a novel nanotheranostic (CPD-protein@BS-qNP), where cetuximab (an FDA-approved antibody drug) was encapsulated within biodegradable silica quenchers (BS-qNP) coated with cell-penetrating poly(disulfide)s (CPDs) (Fig. 21). The silica matrix was further doped with a fluorescent dye (FL-APS 2) and a black hole quencher (BHQ 1-APS 4). By specifically targeting epidermal growth factor receptor (EGFR) on cancer cell surfaces, the loaded cetuximab acted as an effective anticancer drug, avoiding intracellular delivery. The CPD coating prevented internalized cetuximab from lysosomal capture and rapidly disassembled upon exposure to endogenous GSH, maintaining the integrity of the nanotheranostic. Importantly, the inclusion of the fluorescent dye and black hole quencher within Protein@BS-NP enabled the nanoquencher to sense and image cellular hypoxia and protein release. Under hypoxic conditions, the azo portion of BS-NP was reduced by cytochrome P450 reductase, leading to shell disintegration and subsequent release of the antibody and fluorescent dye, thereby efficiently mediating cell state imaging. In fluorescence-triggered testing of the nanotheranostic agent, two control groups were used:

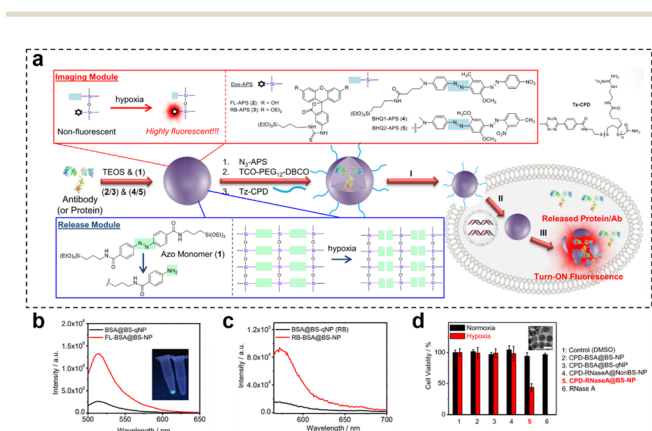


Fig. 21 (a) Preparation of CPD-protein@BS-qNP and the process of its depolymerization and hypoxia-responsive fluorescence release. (b) Fluorescence spectra of BSA@BS-qNP and FL-BSA@BS-NP (0.01 mg mL^{-1}). (c) Fluorescence spectra of BSA@BS-qNP and RB-BSA@BS-NP (0.01 mg mL^{-1}). (d) Cell viability of A549 cells treated with different nanocapsules for 48 h of incubation under hypoxic or normoxic conditions. Reproduced from ref. 81 with permission from Wiley, copyright 2017.

FLProtein@BS-NP and FLProtein@BS-qNP, where FITC-labelled protein was directly encapsulated in nanocapsules without or with quencher 4, respectively. Alternatively, the rhodamine dye RB-APS 3 and the quencher BHQ 1-APS 5 were used, resulting in the corresponding nanocapsules (RBProtein@BS-NP or RBProtein@BS-qNP). The experimental results demonstrated that the nanocapsules had excellent hypoxia-responsive fluorescence turn-on properties. Furthermore, the observation experiment of fluorescence signals revealed a significant cytoplasmic fluorescence increase in hypoxic cells treated with CPD-BSA@BS-qNP, while the nondegradable CPD-BSA@NonBS-qNP exhibited negligible fluorescence. This successful imaging after the degradation of hypoxia-responsive nanocapsules indicated the potential of CPD-protein@BS-qNP as an efficient and promising nanotheranostic agent.

3.1.4. Enzyme. In the TME, specific enzymes, including phospholipase A2 (SPLA-2),⁵ matrix metalloproteinases (MMPs),^{128,129} glutathione S-transferases (GSTs),¹³⁰ and hyaluronidases (HAases),^{131–133} are expressed at elevated levels. Furthermore, degradable silica nanoparticles can be engineered with enzyme-sensitive structures that demonstrate the capacity to achieve controlled drug release by recognizing and responding to these enzymes. Incorporating enzyme-responsive components into the silica framework or grafting enzyme-responsive linkers onto it enables the construction of enzyme-responsive nanotheranostic platforms.

Khashab and coworkers designed enzymatically degradable PSQ nanoparticles using the oxamide bridges present in the organosilica framework.⁹² The degradability of PSQ nanoparticles was then tested in a simulated biological solution. The results indicated that the PSQ nanoparticles were only degraded in the presence of trypsin enzyme in PBS. Furthermore, the PSQ nanoparticles were effectively rendered fluorescence by incorporating fluorescein dyes, enabling the precise imaging of cancer cells. These PSQ nanoparticles distinctly exhibited the characteristic yellow fluorescence attributed to fluorescein, with a light absorption peak at 505 nm, thus showcasing potential suitability for integration within the domain of biomedical diagnostics. To overcome the low mesoporosity, a groundbreaking approach was introduced in the aforementioned study. Mesoporous organosilica nanoparticles (MONs) based on an oxamide phenylene framework were ingeniously engineered through the expert cocondensation of 1,4-bis(triethoxysilyl)-benzene and (*N,N'*-bis(3-(triethoxysilyl)propyl)oxamide) (Fig. 22).¹³⁴ This innovative design strategy led to the creation of MONs, which exhibited a distinctive and unprecedented capability to accommodate considerably higher drug payloads (84 wt%). This signified a monumental stride forward in the realm of drug delivery systems, allowing for the encapsulation of a substantially larger quantity of therapeutic agents within the intricate mesoporous architecture of MONs. This amplified drug-loading prowess holds considerable promise for enhancing therapeutic efficacy while minimizing adverse effects. In essence, this study not only unveiled the ingenious synthesis of oxamide phenylene-based MONs but also shed light on their distinct ability to be enzymatically



Fig. 22 Illustration of the sol-gel synthesis process for MONs and their pore structure before and after protein-mediated degradation (top) or after high drug loading, resulting in nonleaky nanoparticles with uncapped pores (bottom). Reproduced from ref. 134 with permission from Wiley, copyright 2016.

degraded, along with their exceptional drug-loading capabilities. These findings collectively contribute to a transformative advancement in the field of nanomedicine, paving the way for novel and potent strategies in drug delivery and cellular targeting.

Esterase, a pivotal enzyme responsible for catalyzing the breakdown of ester bonds, has emerged as a significant player within the intricate and ever-changing landscape of the TME.^{135,136} This enzyme's pronounced upregulation can be attributed to an interplay of factors, encompassing the heightened metabolic demands of cancer cells, the nuanced shifts in pH equilibrium, and the distinctive biochemical makeup characteristic of the TME.^{5,137} Consequently, the surge in esterase activity presents a captivating avenue for advancing novel cancer therapies and diagnostic methodologies, leveraging its enzymatic prowess to orchestrate targeted and adaptable interventions tailored to the unique intricacies of the tumor milieu. Tsao *et al.*¹³⁸ developed enzymatically degradable polymer/silica hybrid microbubbles (SiPCL) for ultrasound (US) imaging. These SiPCL microbubbles were amenable to conjugation with biomolecules for purposes such as tumor cell imaging, drug loading, and targeted drug delivery. The presence of PCL facilitated the degradation of the microbubbles by high levels of lipase in the TME. To evaluate the US imaging capability, they plotted US image intensity response curves for SiPCL microbubbles with varying feed ratios (ranging from 50 to 95 wt%). The results revealed that as SiPCL feed ratios increased, US image intensity also increased, likely attributed

to the increase in shell elasticity associated with the initial SiPCL content. However, 95 wt% of the SiPCL microbubbles exhibited a minimal response, possibly due to bubble collapse. Electron micrographs of the 95% SiPCL bubbles unveiled their microbubble shells to be very thin (29 nm) while displaying enhanced elasticity. Both *in vitro* and *in vivo* results demonstrated the excellent imaging capabilities of the SiPCL microbubbles, rendering them suitable as ultrasound contrast agents and drug delivery carriers for tumor imaging and treatment.

3.2. Multiple biological triggers

The TME harbours intricate and diverse attributes, encompassing an acidic milieu, elevated redox levels, hypoxia, and aberrant expression of specific enzymes. Through a thorough comprehension and strategic utilization of these distinctive features, the opportunity arises to engineer highly focused nanomedicines or therapeutic systems that are meticulously activated within the TME for precision theranostics. This sophisticated approach not only heightens drug potency but also curtails harm to healthy tissues and alleviates the adverse effects of medications. Furthermore, strategies employing multifaceted triggers inherent to the TME play a pivotal role in surmounting challenges associated with drug resistance. Tumor cells often progressively develop resistance to single therapeutic interventions, leading to a waning efficacy of treatments. By capitalizing on the activation of diverse microenvironmental factors, treatment strategies attain heightened specificity and diversity, ultimately reducing the resistance of tumor cells and amplifying therapy effectiveness. Thus, the advantages derived from harnessing the manifold characteristics of the TME to trigger therapeutic interventions culminate in achieving more accurate and efficient treatment outcomes. This multifaceted approach simultaneously addresses the intricacies of treatment resistance, thereby unveiling the potential for customized therapeutic regimens.

3.2.1. Dual biological triggers

3.2.1.1. Redox and pH. Fluorescence imaging possesses high sensitivity, which makes it a valuable tool in various applications. Li *et al.*¹³⁹ developed a biodegradable and autofluorescent nanoplatform for pH/redox-responsive drug release by constructing disulfide-bonded bridged organosilica (OS) as a carrier for DOX loading. Subsequently, they modified the surface of the OS carrier with dialdehyde dextrin (DAD) through Schiff base bonding and attached cystamine (Cys) to form a DAD/Cys layer, resulting in the preparation of a biodegradable nanoplatform (Dox-loaded OS-N=C-DAD/Cys) (Fig. 23a). The DAD/Cys coating effectively prevented DOX leakage, and its S-S and N=C bonds could be cleaved in reducing and weakly acidic environments, respectively, leading to pH/redox-responsive drug release. Furthermore, the S-S bonds in the OS framework were also susceptible to reduction, leading to redox-responsive degradation of the OS carrier. Additionally, the Schiff base bond exhibited autofluorescence that responded to changes in acidity, serving as a fluorescent probe for real-time monitoring of drug release. *In vitro* experiments demonstrated that the DOX accumulation release was only 6.46%

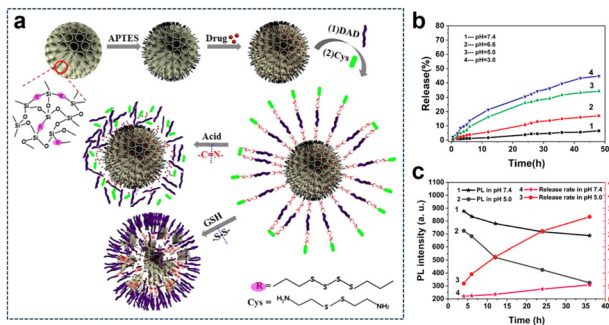


Fig. 23 (a) Preparation and degradation of the DOX-loaded OS-N=C-DAD/Cys system. (b) Cumulative DOX release from OS-N=C-DAD/Cys in PBS under different pH conditions. (c) Relationship between the cumulative release and PL intensity of OS-N=C-DAD/Cys excited at 372 nm in PBS with different pH values. Reproduced from ref. 139 with permission from Elsevier, copyright 2020.

within 48 h at pH 7.4, indicating the effective sealing effect of the DAD/Cys coating. Conversely, under acidic pH conditions, the cumulative drug release amount increased as the pH decreased (Fig. 23b). Quantitative analysis of fluorescence intensity revealed a decrease in fluorescence with decreasing pH in PBS. At pH 5.0, after the drug had been released for 4 h, the fluorescence intensity of the carrier was measured at 724. Subsequently, at 12 h and 36 h of release, the fluorescence intensity of the carrier decreased to 521 and 324, respectively (Fig. 23c).

Magnetic resonance (MR) imaging is a noninvasive, non-ionizing imaging technique that offers high-resolution images, making it a crucial tool in the field of medical imaging. Nonetheless, the clinical utilization of nanoscale contrast agents presents a challenge attributed to their biocompatibility. Premature leakage can potentially cause adverse effects on healthy tissues and compromise the accuracy of imaging results. Therefore, achieving precise delivery and controlled release of these imaging agents is crucial for clinical applications. Zhang *et al.*¹⁴⁰ designed a TME-activated T_1 - T_2 dual-mode MR imaging nanoswitch (PDGFB-FMS). The nanoswitch featured platelet-derived growth factor (PDGFB) conjugated to Fe_3O_4 , which was then coated with Mn-doped silica nanostructures. PDGFB enabled PDGFB-FMS to accumulate in tumors. The acidic and high GSH led to the cleavage of PDGFB-FMS and the release of Fe_3O_4 and Mn^{2+} . This activated the T_1 - T_2 dual-mode MR imaging signal, resulting in a significant enhancement of T_1 and T_2 contrasts (Fig. 24). Experimental results demonstrated that PDGFB-FMS achieved a signal-to-noise ratio of $75.6 \pm 8.8\%$ in T_1 -weighted MRI, which was significantly higher than that of the control group. For T_2 -weighted MR imaging, the maximum signal-to-noise ratios of tumors treated with PDGFB-FMS, FMS, and Fe_3O_4 were 33.3%, 25.7%, and 39.7%, respectively.

Similarly, Yu *et al.*⁶⁶ developed manganese-doped hollow MSNs (Mn-HMSNs) that harnessed the degradability of -Mn-O- linkages in the TME to improve the biodegradability of MSNs (Fig. 25). For improved stability, Mn-HMSNs were

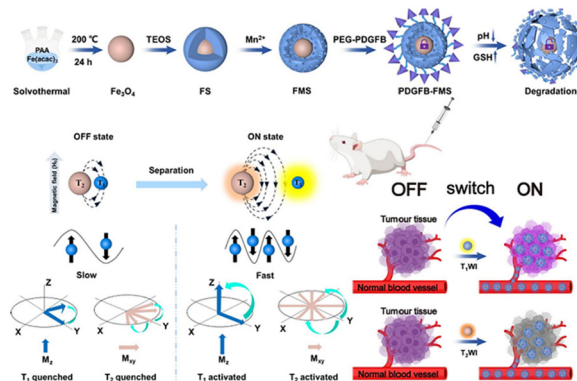


Fig. 24 Schematic synthesis of PDGFB-FMS and mechanism of action as a bimodal MR imaging contrast agent. Reproduced from ref. 140 with permission from Springer Nature, copyright 2023.

PEGylated to obtain PEG/Mn-HMSNs. The tumor's acidic and reductive conditions triggered a “manganese extraction” response in the TME, where manganese oxides dissolved from the Mn-HMSN framework, promoting decomposition and biodegradation, thereby rapidly triggering the release of anticancer drugs. Additionally, manganese ions acted as effective MR contrast agents, enabling integrated tumor diagnosis and therapy. This innovative approach created new possibilities for tumor theranostics, combining drug delivery and imaging in a single platform. The *in vitro* cytotoxicity results of PEG/Mn-HMSNs revealed a high cell viability of 94.9% for HepG2 cells, even at a concentration of $200 \mu\text{g mg}^{-1}$. Furthermore, the DOX-loaded PEG/Mn-HMSNs demonstrated a significant reduction in the cell survival rate compared to an equal concentration of free DOX, highlighting the enhanced therapeutic effect of DOX on HepG2 cells by PEG/Mn-HMSNs.

Sonodynamic therapy (SDT) utilizes ultrasonic methods with enhanced tissue penetration capabilities. In the SDT, a sonosensitizer can convert oxygen into ROS with potent cytotoxic effects, which leads to further hypoxia in the TME, and hypoxia-activated prodrugs (HAPs) could exert a more potent cytotoxic

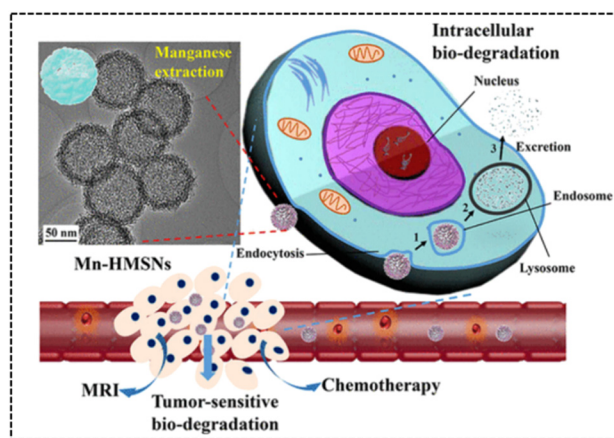


Fig. 25 TEM image and intracellular biodegradation of Mn-HMSNs. Reproduced from ref. 66 with permission from ACS, copyright 2016.

effect within hypoxic environments. The synergistic combination of these two treatment modalities augments the tumor cell-killing efficacy. Wang *et al.*⁷⁰ developed a nanocomposite platform (TPZ@HHSN-C/P-mAb) by synthesizing Ho-doped hollow silica nanospheres sequentially modified with the photosensitizer Ce6 and a monoclonal antibody (mAbPSCA) targeting the prostate stem cell antigen (PSCA). This nanocomposite acted as a carrier for TPZ, effectively delivering it to the tumor region by targeting the overexpressed antigen PSCA on the tumor cell membrane. Additionally, the nanocomposite exhibited ultrasound and MR imaging capabilities. Its hollow structure underwent degradation in the acidic TME. Under ultrasound exposure, HHSN-C/P-mAb consumed oxygen to generate ROS, causing damage to tumor cells, increasing intratumoral hypoxia, and activating the toxicity of TPZ, thus achieving combination therapy with the assistance of imaging (Fig. 26a). The experimental results demonstrated that when the concentration of TPZ@HHSN-C/P-mAb is increased to $200 \mu\text{g mL}^{-1}$, the cell survival rate under US irradiation decreased significantly to only 13.6% (Fig. 26b). Moreover, incubation of Ho-HSN-PEG in an acidic simulated solution at pH 5.2 for a mere 6 h resulted in the appearance of a substantial amount of flocculent on the surface (Fig. 26c). In contrast, no significant change was observed in Ho-HSN-PEG under neutral conditions, thereby confirming the important role of Ho doping in realizing the degradation of the silica framework in acidic environments.

The dual-responsive approach in the TME offers targeted drug release, reducing effects on healthy tissues. It boosts treatment efficacy by activating agents in specific conditions. Li *et al.*¹⁴² synthesized manganese-doped mesoporous silica (MMS) nanospheres to efficiently load DOX. Subsequently, the entire structure was encapsulated with polydopamine (PDA), resulting in the development of a pH/reduction-responsive biodegradable drug delivery system (DOX-MMS/PDA). The MMS nanocarriers exhibited a substantial specific surface area and porous structure, facilitating a remarkable drug loading

capacity for DOX (39.54%). The PDA coating on the external surface of MMS not only effectively prevented the burst drug release but also conferred pH-responsive characteristics onto the nanocarrier, enabling drug release under acidic conditions. Moreover, in the acidic and reducing TME, the Mn–O bond in the MMS nanocarriers underwent cleavage, thereby facilitating the nanocarrier's self-degradation. *In vitro* experiments demonstrated that when the MMS nanocarriers were immersed in PBS with a pH of 5.4 for 2 h, surface degradation commenced, and within 4 h, all mesopores collapsed. In contrast, the degradation process was notably slower when the samples were immersed in PBS with a pH of 7.4. Furthermore, under neutral pH conditions, the cumulative drug release from DOX-MMS/PDA within 48 h remained below 20%, indicating efficient drug encapsulation. As the acidity increased, the cumulative drug release gradually escalated. At pH 2.2, the cumulative amount of the drug released reached 65.0% within 12 h.

Additionally, to overcome drug resistance, Li *et al.*¹⁴¹ developed a versatile small-/macromolecule dual drug delivery system based on the biodegradable organosilica core-shell architecture (Fig. 27a). The small molecule drug was immobilized on the surface of the organosilica shell through pH-responsive imine bonds and was released in the acidic lysosomal environment. Subsequently, the elevated GSH levels within tumor cells triggered the degradation of the organosilica shell, leading to the release of the encapsulated large molecule drug. *In vitro* experiments investigating the acid-responsive drug release of the small molecule FL-C6-NH₂ demonstrated that after 4 h, the cumulative drug release amount reached 20% under acidic conditions (pH = 5.0, 10 mM), and after 24 h, it was approximately 4% under acidic conditions (PBS, pH = 7.4, 10 mM), confirming the targeted release of small molecule drugs under acidic conditions (Fig. 27b). Similarly, in the acidic solution (pH = 5.0) containing 5 mM GSH, the initial release percentage was 6.8%. However, this value rapidly escalated, reaching 41% after 24 h, and further increased to 47% after 48 h (Fig. 27c).

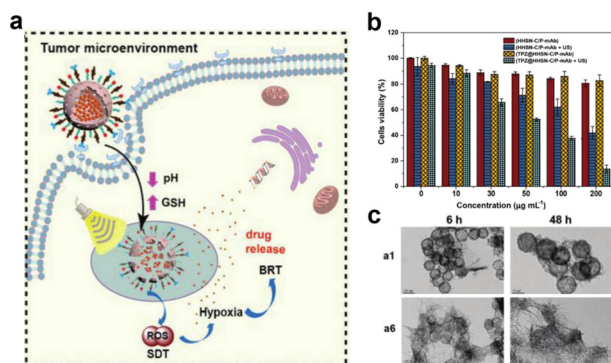


Fig. 26 (a) Application of TPZ@HHSN-C/P-mAb for MR/US imaging and SDT/BRT combination therapy. (b) Viabilities of PC-3 cells after different treatments. (c) TEM images of Ho-HSN-PEG ($100 \mu\text{g mL}^{-1}$) after 6 h and 48 h of incubation with SBFs at different pH and GSH concentrations: (a1) pH = 7.4 (PBS), [GSH] = 0 M; (a6) pH = 5.2 (PBS), [GSH] = 10×10^{-3} M. Reproduced from ref. 70 with permission from Wiley, copyright 2018.

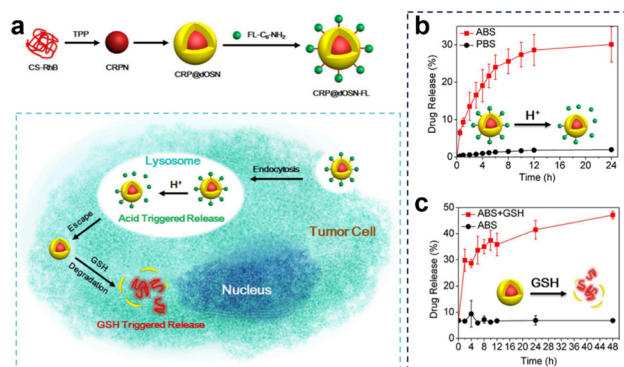


Fig. 27 (a) Preparation of CRP@dOSN-FL loaded with two drugs and its responsive drug release and degradation. (b) *In vitro* release behaviour of FL-C6-NH₂ in the presence of PBS (10 mM, pH = 7.4) and ABS (10 mM, pH = 5.0) at 37 °C. (c) *In vitro* release behaviour of CS-RhB in acidic media (ABS, pH = 5.0) with or without 5 mM GSH. Reproduced from ref. 141 with permission from ACS, copyright 2018.

3.2.1.2. Redox and hypoxia. Glucose, as a vital nutrient, plays a pivotal role in tumor growth. The Warburg effect highlights the dependence of tumor cell proliferation on aerobic glycolysis, rendering tumor cells highly responsive to fluctuations in glucose concentration within their microenvironment. Glucose oxidase (GOx), an enzyme capable of reacting with intracellular glucose, swiftly converts glucose into H_2O_2 and gluconic acid, thus disrupting the energy and nutrient supply within the tumor and inhibiting tumor growth. This presents an opportunity for the development of cancer starvation therapy based on GOx. Moreover, the enzymatic conversion of glucose by GOx into gluconic acid and H_2O_2 consumes oxygen, potentially facilitating a combined approach of hypoxia-based CMT and starvation therapy. Yang *et al.*¹⁴³ developed a novel cascade delivery system that synergistically integrated AQ4N with GOx. AQ4N is an oxygen-sensitive topoisomerase II inhibitor that undergoes activation under hypoxic conditions, transforming into its highly effective anticancer form (AQ4). The yolk-shell structure of tetrasulfide-bridged organosilica nanoparticles (YS-DMONs) exhibited GSH-triggered biodegradability while maintaining a higher drug loading capacity due to their hydrophobic nature (Fig. 28a). Within the TME, the YS-DMONs underwent selective disintegration of their large pore shells, releasing GOx. This, in turn, resulted in the exposure of AQ4N to the hypoxic conditions of the TME, converting it into its cytotoxic form (AQ4) for CMT. Notably, the released GOx effectively depleted the tumor's original glucose, thereby starving the tumor cells and catalyzing the production of H_2O_2 , leading to an oxidative cytotoxic effect. This also contributed to exacerbated tumor hypoxia, preventing insufficient AQ4N activation due to uneven oxygen distribution within the tumor tissue. Moreover, the direct depletion of GSH through tetrasulfide bonds within the nanopreparations prevented the additional loss of H_2O_2 , thereby improving the cell death effect. In cell viability assays, treatment with YS-DMONs-AQ4N-GOx under simulated normoxic (20% O_2) and hypoxic (2% O_2) conditions resulted in cell viabilities of only 9.2% and 5.0%, respectively (Fig. 28b and c).

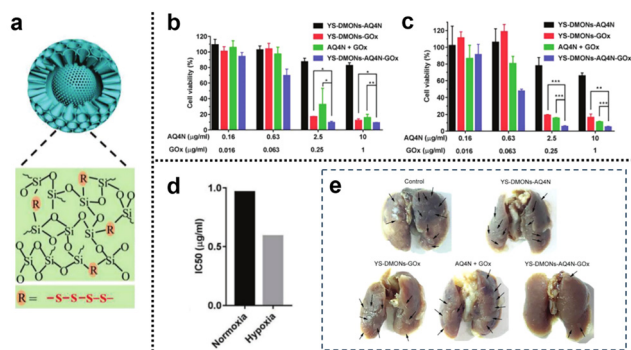


Fig. 28 (a) YS-DMONs with a tetrasulfide incorporated framework. (b) and (c) Cell viability of 4T1 cells after different treatments under normoxic and hypoxic conditions for 48 h. (d) IC₅₀ values of YS-DMON-AQ4N-GOx against 4T1 cells under normoxic and hypoxic conditions. (e) Tumor nodules in the lungs after different treatments. Reproduced from ref. 143 with permission from Wiley, copyright 2018.

The calculated IC₅₀ of AQ4N in the YS-DMONs-AQ4N-GOx under normoxic conditions ($0.96 \mu\text{g mL}^{-1}$) was higher than that under hypoxic conditions ($0.59 \mu\text{g mL}^{-1}$), further confirming the high efficacy of AQ4N under hypoxic conditions (Fig. 28d). Additionally, *in vivo* experiments demonstrated that YS-DMON-AQ4N-GOx significantly reduced tumor nodules and exhibited remarkable inhibitory effects on lung metastasis compared to the control groups (YS-DMON-AQ4N, YS-DMON-GOx, and AQ4N + GOx) (Fig. 28e).

3.2.1.3. Redox and enzyme. Glutathione S-transferases π (GST π), which are highly expressed in hepatocellular carcinoma cells (HCC), are up to 4–5 times higher than those in normal cells.¹³⁰ Based on this, an enzyme/redox dual-responsive nanodrug (QM-NPQ@PDHN) was developed by Jia *et al.* through a prodrug loading strategy (Fig. 29a).¹⁴⁴ This nanodrug achieved the controlled release of nitric oxide (NO) in response to the activity of GST π and GSH within the TME, resulting in effective suppression of tumor growth. Moreover, the nanodrug was thoughtfully designed with switchable size and charge properties, enabling efficient penetration and internalization within the tumor tissue. The integration of the fluorescent molecule QM-2 facilitated real-time tracking and assessment of its targeting efficacy *in vivo*. The tumor-targeting efficacy of QM-NPQ@PDHN was assessed using fluorescence imaging, and a nude mouse model was established by inoculating SMMC-7721 tumors and administering QM-NPQ@PDHN *via* the tail vein.

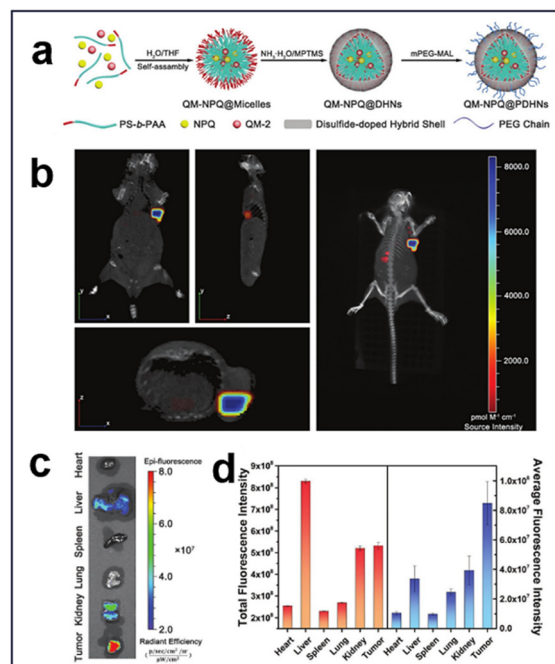


Fig. 29 (a) Schematic synthesis of QM-NPQ@PDHNs. (b) Three-dimensional fluorescence images of hormonal mice at 24 h after intravenous injection of QM-NPQ@PDHNs. (c) *Ex vivo* fluorescence images of each organ at 24 h after intravenous injection of QM-NPQ@PDHNs. (d) Fluorescence intensity of tumors and organs in mice killed at 24 h after intravenous injection of QM-NPQ@PDHNs. Reproduced from ref. 144 with permission from Wiley, copyright 2018.

The biodistribution of QM-NPQ@PDHN was investigated *in vivo* through fluorescence imaging employing the IVIS system, revealing robust fluorescence at the tumor site (Fig. 29b). 24 h after QM-NPQ@PDHN injection, the mice were euthanized, and *ex vivo* fluorescence imaging was conducted on major organs and tumor tissues. The results indicated weak fluorescence in tumor tissues, liver, and kidney (Fig. 29c). Predominant accumulation of QM-NPQ@PDHN in the liver, kidney, and tumor tissues was demonstrated through semi-quantitative analysis of the average fluorescence intensity distribution, with significantly higher levels in the tumor tissues than in other organs (Fig. 29d).

3.2.2. Triple biological triggers

3.2.2.1. Redox, hypoxia, and enzyme. HAPs represent a novel class of therapeutic agents meticulously designed to target and activate specifically within the hypoxic regions of the TME.^{145,146} These prodrugs are engineered to remain inactive or minimally toxic in oxygen-rich (normoxic) environments. However, upon encountering the hypoxic TME, they undergo specific chemical transformations or enzymatic reactions that trigger the release of their active drug forms. This activation process occurs exclusively within the hypoxic regions of the tumor, sparing healthy tissues from unnecessary drug exposure. A common strategy employed in HAPs involves incorporating nitroaromatic compounds into the prodrug structure. Inside the hypoxic TME, nitroreductase enzymes present in tumor cells metabolize nitro groups from HAPs, leading to the liberation of potent cytotoxic agents. Consequently, tumor cells are selectively targeted and destroyed, bolstering the effectiveness of cancer treatment while minimizing harm to normal tissues. Currently, a series of HAPs have been developed for cancer treatment, including banoxantrone (AQ4N) and tirapazamine (TPZ). Cheng *et al.*¹⁴⁷ developed a novel nanohybrid (HA-TPZ&IR@GMON) for synergistic cancer therapy (Fig. 30). This nanohybrid involved the incorporation of photosensitizers IR820 and TPZ into GSH-degradable mesoporous organic silica nanoparticles (GMONs), which were then coated with HA. HA played a crucial role as a CD44 receptor-targeting agent,

enabling specific and precise targeting of tumor tissues by the nanohybrid. Upon exposure to HAase and GSH, HA and GMON experienced controlled degradation, facilitating the release of IR820 and TPZ. IR820 induced PDT by generating $^1\text{O}_2$ upon NIR laser irradiation, concurrently depleting oxygen, thereby intensifying the hypoxic state of the tumor tissue. Moreover, TPZ exhibited enhanced activation under highly hypoxic conditions, thereby augmenting the efficacy of CMT. *In vitro* experiments demonstrated that treatment with $200\ \mu\text{g mL}^{-1}$ HATPZ&IR@GMON for 5 min under NIR laser ($1\ \text{W cm}^{-2}$) irradiation resulted in a cell survival rate of less than 10%. Additionally, in the absence of NIR laser irradiation, 36% of cells survived after treatment with $200\ \mu\text{g mL}^{-1}$ HA-TPZ@GMON. Furthermore, under NIR laser irradiation, HA-TPZ&IR@GMONs induced apoptosis in 36.2% of 4T1 cells under normoxic conditions and a remarkable 73.4% of cells in a hypoxic environment.

3.2.2.2. pH, redox, and enzyme. HAase is highly expressed in the TME, facilitating the degradation of HA to induce the disintegration of nanoplateforms.^{148,149} Consequently, researchers have actively pursued the development and design of numerous HA-modified nanosystems, strategically targeting tumor cells that exhibit high expression of CD44 molecules on their cell membranes.^{150,151} Yang *et al.*¹⁵² developed a tumor immunotherapy strategy for triple-negative breast cancer (TNBC), addressing challenges such as high recurrence, poor prognosis, and limited treatment options. Their approach combined mild PTT and nanocatalytic drug action using Fe-loaded mesoporous organosilica (MOF) nanoparticles, with ICG as a photothermal agent and HA as a drug carrier (IMOFH) (Fig. 31). HA incorporation enabled IMOFH to specifically target CD44 molecules on 4T1 breast cancer cells, leading to highly targeted accumulation at the tumor site. The presence of HAase in the TME facilitated drug internalization by promoting HA degradation. Moreover, IMOFH exhibited pH- and GSH-responsive behaviour in the TME. Upon reaching the TME, IMOFH underwent structural degradation, releasing Fe^{3+} and

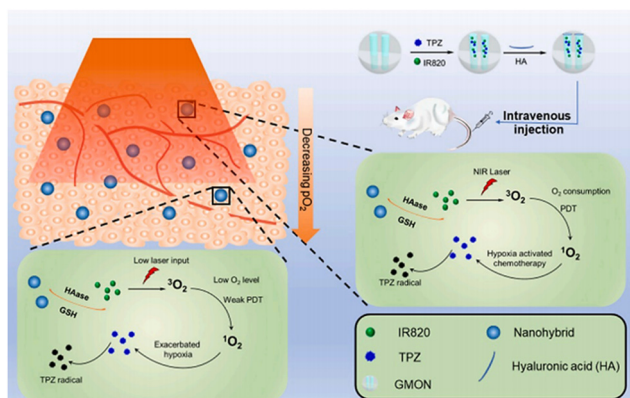


Fig. 30 Schematic representation of the anticancer mechanism of HA-TPZ&IR@GMONs. Reproduced from ref. 147 with permission from Elsevier, copyright 2021.

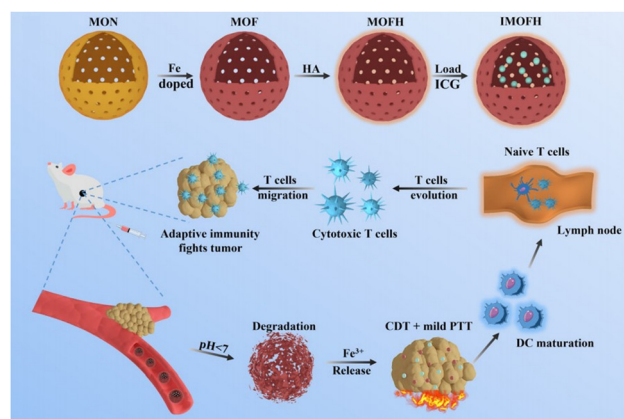


Fig. 31 Preparation and antitumour scheme of IMOFH. Reproduced from ref. 152 with permission from the Royal Society of Chemistry, copyright 2022.

ICG. Under NIR laser irradiation, ICG demonstrated excellent photothermal conversion ability, enabling mild PTT. Additionally, the Fe^{3+} Fenton reagent, released from IMOFH, triggered the generation of ROS by exploiting H_2O_2 within the TME. This ROS generation acted synergistically with mild PTT. This ROS-induced oxidative activity could also trigger immunogenic cell death (ICD) in tumor cells,¹⁵³ releasing damage-associated molecular patterns (DAMPs) such as ATP and HMGB1. This process activates dendritic cells, preventing T-cell exhaustion and tumor cell immune evasion and increasing T-cell levels in the TME, thereby enhancing the body's immune capacity. The researchers evaluated the pH and GSH responsiveness of IMOFH, noting partial degradation on the third day and nearly complete degradation on the seventh day in an acidic (pH 6.5) and GSH (10 mM) solution. They also assessed the photothermal ability of the IMOFH using thermal imaging technology (808 nm), finding its concentration-dependent and light power-dependent heating abilities. Higher IMOFH concentrations and greater light power resulted in stronger heating effects. To confirm the targeted accumulation of IMOFH in 4T1 breast cancer, Cy5.5-labelled MOFH was intravenously injected into mice bearing 4T1 tumors. The results demonstrated time-dependent enhancement of the fluorescence signal in the 4T1 tumor site, peaking at 8 h after injection. After 24 h, they performed *ex vivo* fluorescence imaging of major organs and 4T1 tumors, revealing significantly higher signal intensities in the liver and 4T1 tumors than in other tissues. These findings highlighted the excellent tumor accumulation ability of IMOFH, positioning it as a promising therapeutic agent for TNBC.

In addition, Shi *et al.*¹⁵⁴ developed an intelligent pH-responsive nanoplatform (HSPMH-DOX) for MR imaging-guided synergistic chemo-photothermal therapy and CDT (Fig. 32a). Initially, DOX-loaded hollow mesoporous silica nanoparticles (HSP-DOX) were prepared. Then, dopamine, with photothermal conversion performance and pH responsiveness, was used to coat the HSP-DOX and act as a “controlled gate” for drug release. Subsequently, a layer of manganese dioxide nanosheets was grown on the surface of HSP-DOX through *in situ* potassium permanganate reduction, introducing Mn-O bonds into the -Si-O-Si- framework to alter mesoporous silica biodegradability. Simultaneously, the surface was functionalized with the targeting group HA to form HSPMH-DOX, enabling specific recognition of tumor cells and tissues. In the acidic TME, the MnO_2 nanosheets could be converted into Mn^{2+} through a reduction reaction that provided a higher longitudinal relaxivity (T_1), improving the accuracy of tumor localization. The *in vitro* MR imaging results of HSPMH under varying pH conditions indicated no significant difference in the MR imaging signal at pH 7.4 (Fig. 32b). However, a noticeable signal enhancement was observed at pH 5.5, leading to a considerable improvement in T_1 -MR contrast within the tumor (Fig. 32c).

MMPs possess the capacity to degrade extracellular matrix proteins such as collagen and fibronectin, alongside other molecules in the extracellular milieu.^{155,156} The enzymatic

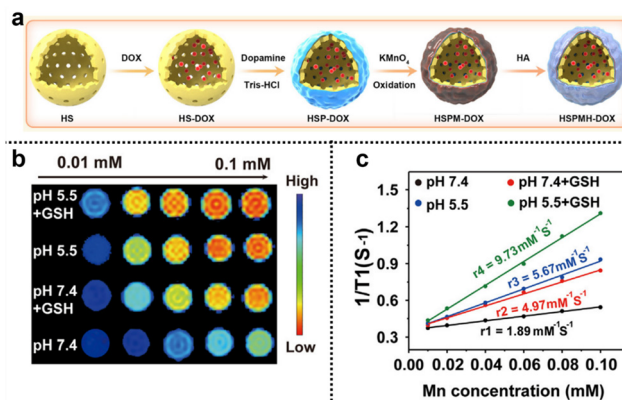


Fig. 32 (a) Schematic representation of the preparation of HS@PDA/ MnO_2 /HA-DOX (HSPMH-DOX) and its TME responsive activation for MRI and synergistic therapy. (b) and (c) MR images of the T_1 map and T_1 reflexivity of HSPMH under different conditions and concentrations. Reproduced from ref. 154 with permission from Elsevier, copyright 2023.

activity of MMPs undergoes meticulous regulation across multiple tiers, encompassing transcription, translation, and activation processes.^{157–160} Normally, MMPs maintain a subdued activity level, serving to uphold extracellular matrix stability. However, within the TME, numerous factors, including the secretion of growth factors, modifications in the ECM composition, and atypical expression by tumor cells, can culminate in the excessive upregulation and activation of MMPs.¹⁶¹ Hence, the strategic modification of degradable silica nanoparticles with MMP-sensitive peptide sequences enables the effective and targeted delivery of nanodrugs, facilitating precise imaging and treatment of tumors. Xiao *et al.*¹⁶² developed a gelatin-based nanocluster (DOX-icluster) with dual-sized/charge-switchable and multiresponsive characteristics for targeted antitumour therapy (Fig. 33). The formation of the nanocluster involved the electrostatic assembly of FA-modified gelatin (FA-GelDMA). This gelatin was sensitive to MMP and was combined with small-sized NH_2 -modified hollow mesoporous organosilica nanoparticles loaded with DOX (DOX-HMON- NH_2). The distinctive feature of DOX-icluster lies in the incorporation of disulfide bonds into its silica framework, imparting responsiveness to intracellular GSH and leading to rapid degradation, rendering it highly biodegradable.^{80,85} Additionally, the DOX-icluster demonstrated switchable sizes and charges that facilitated tumor cell internalization. Under neutral conditions, DOX-iclusters exhibited a size of approximately 199 nm. However, in the acidic TME, the dimethylamino methylene bonds within FA-GelDMA were cleaved, resulting in gelatin hydrolysis facilitated by overexpressed MMP. This process led to the release of DOX-HMON- NH_2 nanoparticles (approximately 48 nm), which effectively accumulated in tumors and promoted cellular internalization. Intracellularly, DOX-HMON- NH_2 was subsequently broken down by intracellular GSH, leading to DOX release at an approximate cumulative release amount of 48.1% and exerting its chemotherapeutic antitumour effect. The tumor inhibition experiments revealed that under conditions of pH = 6.5 and in the presence of MMP-2, the

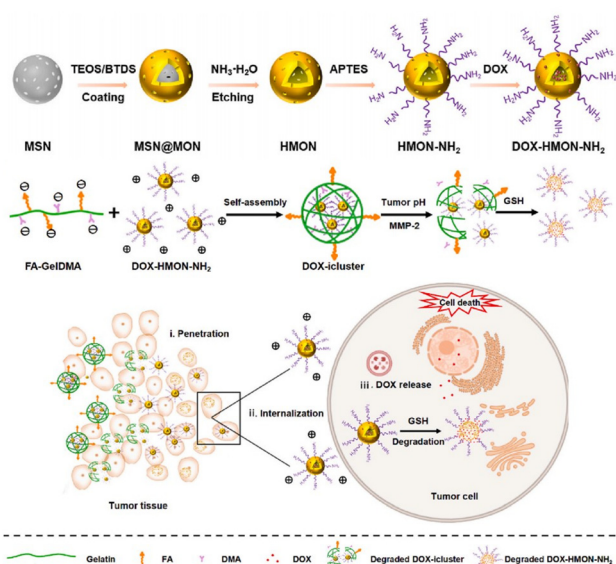


Fig. 33 Schematic diagram of the synthesis and antitumour effects of DOX-HMON-NH₂. Reproduced from ref. 162 with permission from Elsevier, copyright 2023.

DOX-icluster exhibited the strongest tumor inhibition effect, reducing the tumor volume to 15.1% of the initial volume on the seventh day.

3.2.2.3. pH, redox, and hypoxia. The utilization of HAPs as a promising oncotherapy strategy is impeded by the limitations arising from insufficient tumor hypoxia. Furthermore, standalone prodrugs may not effectively combat the complexity of tumors. To overcome these challenges, Hu *et al.*¹⁶³ developed a novel nanosystem (TPZ@FeMSN-GOX) that integrated triple synergistic cancer starvation therapy, hypoxia-activated CMT, and CDT (Fig. 34a). The fabrication of TPZ@FeMSN-GOX involved the synthesis of iron-doped mesoporous silica nanoparticles (FeMSNs), conjugation with GOX on the surface, and subsequent loading with TPZ. The introduction of iron in this nanosystem facilitated its potential for the Fenton reaction, while TPZ underwent transformation into the cytotoxic therapeutic agent TPZ radical under low oxygen conditions, precisely damaging cancer cells and reducing side effects on normal tissues. Upon entering the tumor, TPZ@FeMSN-GOX utilized GOX to induce starvation therapy and produce H₂O₂, which in turn consumed O₂, intensifying the hypoxic environment and thereby enhancing TPZ-mediated CMT. Additionally, the released Fe³⁺ was reduced to Fe²⁺ by GSH, further converting H₂O₂ into highly toxic •OH through the Fenton reaction and activating CDT. Moreover, continuous H₂O₂ production and glucose consumption amplified the acidic environment, ensuring a sustained and effective Fenton reaction. *In vitro* experiments demonstrated that TPZ@FeMSN-GOX substantially reduced the cell viability of both PANC-1 and 4T1 cells. Even at low concentrations of 2.5 μg mL⁻¹ and after 24 h of incubation, cell viability was markedly reduced to 45.26% and 48.59%, respectively, underscoring its impressive anticancer efficacy

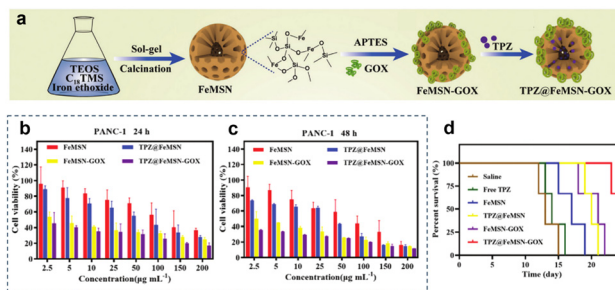


Fig. 34 (a) Schematic representation of the preparation process of TPZ@FeMSN-GOX. (b) and (c) Cell viability of PANC-1 cells after incubation with different concentrations of samples for 24 h and 48 h. (d) Survival curves of 4T1 tumor-bearing mice after different treatments. Reproduced from ref. 163 with permission from the Royal Society of Chemistry, copyright 2022.

(Fig. 34b and c). *In vivo* experiments revealed that mice treated with saline and free TPZ exhibited rapid tumor growth, indicating that TPZ alone was not sufficient to yield antitumour effects. In contrast, mice treated with TPZ@FeMSN exhibited partially inhibited tumor growth, whereas TPZ@FeMSN-GOX demonstrated the most substantial effect in suppressing tumor growth in mice. Remarkably, the mice treated with TPZ@FeMSN-GOX survived the longest (25 days) compared to the other groups (Fig. 34d).

3.2.3. Quadruple biological triggers. Yan *et al.*¹⁶⁴ developed a novel core-shell nanosystem (AD-Cu-DOX-HA) that consisted of an AIE-active photosensitizer, copper ion-engineered amino-silica, a direct coordination polymer of DOX, and HA (Fig. 35). The core component, MeOTTVP, served as an active photosensitizer, contributing to the regulation of the nanomaterial's structure and providing NIR fluorescence with AIE functionality. This feature enabled the generation of ROS such as •OH and ¹O₂ for effective PDT when exposed to NIR laser irradiation. Furthermore, through coordination with Cu²⁺, the low cross-linking density of the core allowed Cu²⁺ to infiltrate into the inner structure, facilitating the incorporation of DOX and inducing a redshift in the absorption peak of DOX. This resulted in significant fluorescence quenching and rendered DOX nonfluorescence, making it an ideal candidate for precise drug delivery and controlled release. Moreover, the AD-Cu core-shell structure exhibited acid-responsive degradability, enhancing its therapeutic efficiency within the acidic TME. To achieve targeted delivery, the nanosystem was further modified with HA, which specifically binds to CD44 molecules overexpressed on cancer cell membranes. This unique targeting capability enabled selective accumulation of the nanosystem in the TME, maximizing its therapeutic effects while minimizing off-target side effects. Upon administration, the overexpressed HAase in the TME facilitated the degradation of HA, promoting the cellular uptake of AD-Cu-DOX. Experimental results confirmed that AD-Cu-DOX-HA was internalized into cells *via* endocytosis and accumulated within lysosomes. In the acidic lysosomal environment, the AD-Cu core underwent disintegration, resulting in the release of MeOTTVP and encapsulated DOX. Cu²⁺ was

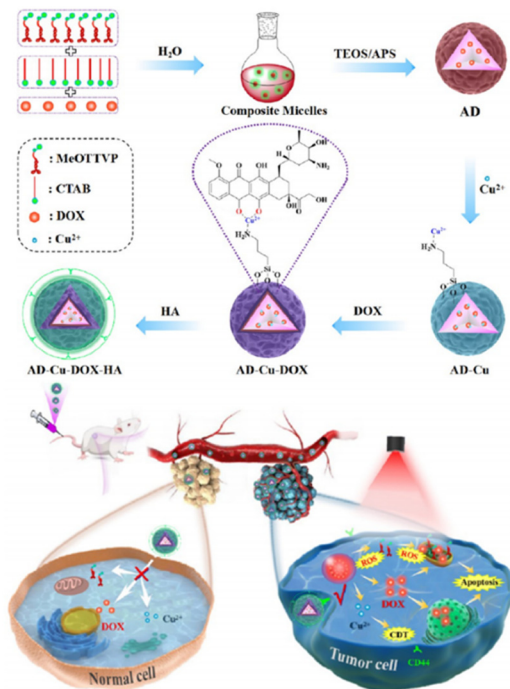


Fig. 35 Preparation process of core-shell AD-Cu-DOX-HA and its further application in targeted and tumor-specific therapy. Reproduced from ref. 164 with permission from ACS, copyright 2022.

gradually released within the cells, and these ions could be converted to Cu^+ by GSH in tumor cells. Subsequently, Cu^+ could effectively generate ROS through a Fenton-like reaction. To enhance the photodynamic effect, the encapsulated photosensitizer MeOTTVP exhibited effective internalization within lysosomes and subsequent accumulation in mitochondria upon release. Upon exposure to light irradiation, AD-Cu-DOX-HA induced multiple subcellular damage pathways, resulting in a significant acceleration of cancer cell death through synergistic PDT, CDT, and CMT. Furthermore, DOX present in lysosomes escaped and entered the mitochondria, where it activated mitochondrial NADPH oxidase 4 (NOX 4) to induce H_2O_2 generation, thereby assisting Cu^{2+} -mediated CDT. In addition to its therapeutic effects, AD-Cu-DOX-HA also exhibited fluorescence imaging capability.

Wang *et al.*¹⁶⁵ developed synergistic therapeutic nanoplat-forms (DCI) for the combination of the PDT and the CDT. The nanoplat-forms utilized dithioether-crosslinked dendritic mesoporous organosilica (DMOS) as a carrier to load copper peroxide (CuO_2) and a photosensitizer ICG, which was further modified with HA (Fig. 36). HA exhibited specific binding affinity towards CD44 molecules commonly overexpressed on cancer cell membranes. This selective interaction allowed DCI to achieve high accumulation within tumor tissues, thereby facilitating precise and targeted drug delivery. Specifically, under acidic conditions, DCI could effectively release $\text{H}_2\text{O}_2/\text{O}_2$ while depleting GSH, thus effectively targeting the specific conditions of the TME. Furthermore, the released Cu^{2+} served as a valuable agent for T_1 -weighted MR imaging, enabling both *in vitro* and *in vivo*

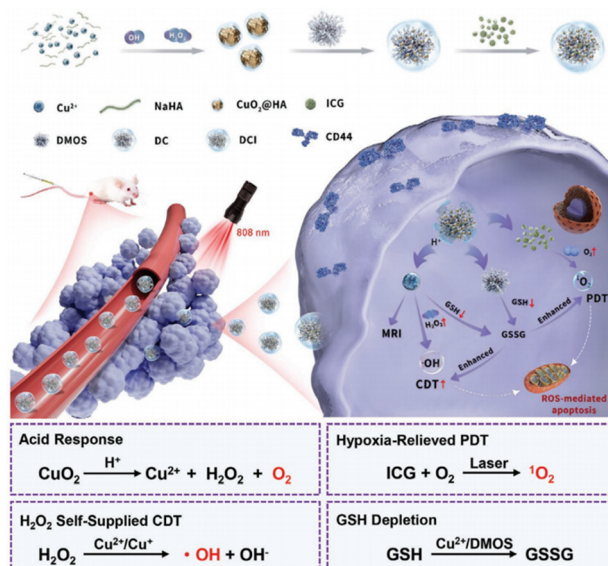


Fig. 36 Principled process for MRI-guided PDT combined with CDT of DMOS@ CuO_2 /ICG-HA (DCI). Reproduced from ref. 165 with permission from Wiley, copyright 2022.

imaging for guided therapies. Upon accumulation at the tumor site, DCI adeptly surmounted the challenge of hypoxia and induced a substantial elevation of ROS upon NIR laser irradiation. This ROS generation led to the apoptotic demise of tumor cells, resulting in a significant amplification of therapeutic efficacy against cancer. The results clearly demonstrated the antitumour efficacy of DCI, as evidenced by the DCI + NIR treatment, which exhibited minimal fluctuations in body weight and the smallest tumour volume. The MR imaging performance of DCI was assessed, revealing a significant enhancement of MR imaging signals at the tumor after intravenous administration. The *in vitro* MR imaging signal intensity exhibited a concentration dependency at acidic pH (pH = 5.5), with higher DCI concentrations resulting in increased intensity. In contrast, the MR imaging signal intensity remained relatively constant at pH = 7.4, regardless of the variations in DCI concentrations.

4. Conclusions and future perspectives

We have presented a comprehensive overview of the classification and degradation mechanism of degradable silica nanoparticles, and these nanoparticles were designed to respond to specific TME stimuli, including pH, redox, hypoxia, and enzymes, for precision tumor diagnosis and therapy. We emphasize the importance of designing degradable nanoplat-forms to mitigate potential toxic side effects *in vivo*. The degradable silica nanoparticles discussed not only exhibit efficient clearance and low toxicity but also offer controlled drug release, improved imaging capabilities, and enhanced therapeutic effects, thereby presenting promising prospects

for cancer theranostics. However, the development of TME-responsive precision diagnosis and therapy based on degradable silica nanoparticles faces several challenges. While the potential of degradable silica nanoparticles for TME-responsive precision theranostics is promising, several challenges must be addressed.

First, the preparation of most degradable silica nanoparticles presents challenges, including high difficulty, complex processes, and high costs, which partly restrict their application in the biomedical field. Regarding imaging, there is a lack of rational design to optimize imaging performance and enhance imaging quality in deep tissues. As carriers for drugs, the stability of degradable silica nanoparticles loaded with drugs requires further improvement. Furthermore, to address the TME, the rational design of highly responsive or multi-responsive nanoplatfoms, along with the development of intelligent nanomaterials integrating endogenous responses and exogenous stimuli (*e.g.*, light, X-rays, magnetic field, *etc.*), prove to be valuable in achieving precise tumor therapy, thereby enhancing drug utilization and theranostic efficacy.

Second, the complexity and specificity of the TME often hinder the attainment of optimal therapeutic effects and may even contribute to drug resistance, recurrence, and metastasis. The features of the TME extend beyond those mentioned; researchers have reported immune suppression, inflammation, and cytokine production. The development of more precise TME-responsive strategies and the achievement of specific responses to TME continue to be challenges for researchers. Additionally, the TME closely influences the survival, invasion, and metastasis of tumor cells. Presently, the treatment efficacy for highly resistant tumors remains unsatisfactory. Despite the enhanced penetration and drug accumulation in tumor regions through the use of degradable silica nanoparticles, the high drug resistance and efflux in numerous tumor cells continue to limit treatment effectiveness. Thus, more effective measures are needed to augment drug uptake by tumor cells and prevent tumor cell migration.

Third, the safe application of degradable silica nanoparticles should be ensured. Preliminary results demonstrate the potential of degradable silica nanoparticles for future disease treatment. However, further research is imperative to ensure their safe application in clinical settings. The degradation effects of silica nanoparticles under various physiological conditions within the body need examination. Additionally, the ions generated after material degradation may cause damage to corresponding organs during metabolism. Therefore, systematic and long-term research is required to investigate the biological distribution, circulation, metabolism, degradation, and excretion of these degradable silica nanoparticles.

TME-responsive precision diagnosis and therapy utilizing degradable silica nanoparticles hold immense potential and broad prospects. However, overcoming challenges in their development and understanding their behaviour within the biological system are crucial. Further in-depth research will strengthen the control and modification of degradable silica nanoparticles and enhance our ability to achieve their true

potential in tumor diagnosis and treatment, ultimately contributing to advancements in human health.

Author contributions

Junjie Zhang: writing – original draft, supervision, writing – review & editing, funding acquisition. Kaiyuan Tang: investigation, writing – original draft. Zilu Liu: writing – original draft, formal analysis, visualization. Zhijing Zhang: investigation, formal analysis, visualization. Shufan Duan: formal analysis, visualization. Hui Wang: investigation, visualization. Hui Yang: formal analysis, visualization. Dongliang Yang: conceptualization, formal analysis, project administration, writing – review & editing. Wenpei Fan: conceptualization, project administration, writing – review & editing, funding acquisition.

Conflicts of interest

The authors declare no conflicts of interest.

Acknowledgements

This work was supported by the Department of Education of Anhui Province (KJ2021A0732), the open research fund of State Key Laboratory of Organic Electronics and Information Displays (SKL2023002), the Funding of Double First-Rate Discipline Innovation Team of China Pharmaceutical University (CPUQNJ22_04), the Fundamental Research Funds for the Central Universities of China (2632023TD01), the Science and Technology Innovation Guidance Project of Bengbu City (20220127), and the National College Students' Innovation and Entrepreneurship Training Program (202210367075).

Notes and references

- 1 J. Cortes, J. M. Perez-Garcia, A. Llombart-Cussac, G. Curigliano, N. S. El Saghir, F. Cardoso, C. H. Barrios, S. Wagle, J. Roman, N. Harbeck, A. Eniu, P. A. Kaufman, J. Tabernero, L. Garcia-Estevéz, P. Schmid and J. Arribas, *Ca-Cancer J. Clin.*, 2020, **70**, 105–124.
- 2 T. Wu and Y. Dai, *Cancer Lett.*, 2017, **387**, 61–68.
- 3 N. M. Anderson and M. C. Simon, *Curr. Biol.*, 2020, **30**, R921–R925.
- 4 R. Baghban, L. Roshangar, R. Jahanban-Esfahlan, K. Seidi, A. Ebrahimi-Kalan, M. Jaymand, S. Kolahian, T. Javaheri and P. Zare, *Cell Commun. Signaling*, 2020, **18**, 59.
- 5 F. Gong, N. Yang, X. Wang, Q. Zhao, Q. Chen, Z. Liu and L. Cheng, *Nano Today*, 2020, **32**, 100851.
- 6 Y. Dai, C. Xu, X. Sun and X. Chen, *Chem. Soc. Rev.*, 2017, **46**, 3830–3852.
- 7 M. O. Li, N. Wolf, D. H. Raulet, L. Akkari, M. J. Pittet, P. C. Rodriguez, R. N. Kaplan, A. Munitz, Z. Zhang, S. Cheng and N. Bhardwaj, *Cancer Cell*, 2021, **39**, 725–729.
- 8 X. Wang, Z. Chen, J. Xu, S. Tang, N. An, L. Jiang, Y. Zhang, S. Zhang, Q. Zhang, Y. Shen, S. Chen, X. Lan, T. Wang,

- L. Zhai, S. Cao, S. Guo, Y. Liu, A. Bi, Y. Chen, X. Gai, Y. Duan, Y. Zheng, Y. Fu, Y. Li, L. Yuan, L. Tong, K. Mo, M. Wang, S. H. Lin, M. Tan, C. Luo, Y. Chen, J. Liu, Q. Zhang, L. Li and M. Huang, *Cell Res.*, 2022, **32**, 638–658.
- 9 J. Qin, H. Tian, F. Kong, Y. Guo, W. Du, C. Zhang, H. Gu and Y. Li, *Sens. Actuators, B*, 2022, **371**, 132522.
- 10 C. Michiels, C. Tellier and O. Feron, *Biochim. Biophys. Acta, Bioenerg.*, 2016, **1866**, 76–86.
- 11 Y. Luo, C. Li, Y. Zhang, P. Liu, H. Chen, Z. Zhao, Y. Wang, Z. Zhou, H. Song, B. Su, C. Li, X. Li, T. Zhang, H. You, Y. Wu, Z. Tian, S. Zhang, Y. Guo, H. Fan, Q. Chen, C. Jiang and T. Sun, *Acta Biomater.*, 2023, **167**, 387–400.
- 12 R. McShane, S. Arya, A. J. Stewart, P. D. Caie and M. Bates, *Biochim. Biophys. Acta, Rev. Cancer*, 2021, **1876**, 188598.
- 13 Z. Zhang, C. Ding, T. Sun, L. Wang and C. Chen, *Adv. Healthcare Mater.*, 2023, **12**, e2300153.
- 14 D. A. Snellings, C. C. Hong, A. A. Ren, M. A. Lopez-Ramirez, R. Girard, A. Srinath, D. A. Marchuk, M. H. Ginsberg, I. A. Awad and M. L. Kahn, *Circ. Res.*, 2021, **129**, 195–215.
- 15 B. C. Ozdemir, T. Pentcheva-Hoang, J. L. Carstens, X. Zheng, C. C. Wu, T. R. Simpson, H. Laklai, H. Sugimoto, C. Kahlert, S. V. Novitskiy, A. De Jesus-Acosta, P. Sharma, P. Heidari, U. Mahmood, L. Chin, H. L. Moses, V. M. Weaver, A. Maitra, J. P. Allison, V. S. LeBleu and R. Kalluri, *Cancer Cell*, 2014, **25**, 719–734.
- 16 S. Turajlic, A. Sottoriva, T. Graham and C. Swanton, *Nat. Rev. Cancer*, 2019, **20**, 404–416.
- 17 S. Gavas, S. Quazi and T. M. Karpinski, *Nanoscale Res. Lett.*, 2021, **16**, 173.
- 18 B. Peltanova, M. Raudenska and M. Masarik, *Mol. Cancer*, 2019, **18**, 63.
- 19 J. Fang, W. Islam and H. Maeda, *Adv. Drug Delivery Rev.*, 2020, **157**, 142–160.
- 20 J. K. Tee, L. X. Yip, E. S. Tan, S. Santitewagun, A. Prasath, P. C. Ke, H. K. Ho and D. T. Leong, *Chem. Soc. Rev.*, 2019, **48**, 5381–5407.
- 21 W. Ying, Y. Zhang, W. Gao, X. Cai, G. Wang, X. Wu, L. Chen, Z. Meng, Y. Zheng, B. Hu and X. Lin, *ACS Nano*, 2020, **14**, 9662–9674.
- 22 L. Gong, Y. Zhang, J. Zhao, Y. Zhang, K. Tu, L. Jiao, Q. Xu, M. Zhang and S. Han, *Small*, 2022, **18**, 2107656.
- 23 X. Kong, Y. Qi, X. Wang, R. Jiang, J. Wang, Y. Fang, J. Gao and K. C. Hwang, *Prog. Mater. Sci.*, 2023, 101070.
- 24 A. Gulzar, J. Xu, C. Wang, F. He, D. Yang, S. Gai, P. Yang, J. Lin, D. Jin and B. Xing, *Nano Today*, 2019, **26**, 16–56.
- 25 C. S. Sia, H. P. Lim, B. T. Tey, B. H. Goh and L. E. Low, *Biochim. Biophys. Acta, Rev. Cancer*, 2022, **1877**, 188779.
- 26 J. G. Croissant, Y. Fatieiev and N. M. Khashab, *Adv. Mater.*, 2017, **29**, 1604634.
- 27 J. Liu, M. Yu, C. Zhou and J. Zheng, *Mater. Today*, 2013, **16**, 477–486.
- 28 Y. Tan, M. Chen, H. Chen, J. Wu and J. Liu, *Angew. Chem., Int. Ed.*, 2021, **60**, 11713–11717.
- 29 B. Du, M. Yu and J. Zheng, *Nat. Rev. Mater.*, 2018, **3**, 358–374.
- 30 X. Wang, X. Zhong, J. Li, Z. Liu and L. Cheng, *Chem. Soc. Rev.*, 2021, **50**, 8669–8742.
- 31 N. Senthilkumar, P. K. Sharma, N. Sood and N. J. C. C. R. Bhalla, *Coord. Chem. Rev.*, 2021, **445**, 214082.
- 32 N. Feliu, D. Docter, M. Heine, P. Del Pino, S. Ashraf, J. Kolosnjaj-Tabi, P. Macchiarini, P. Nielsen, D. Alloyeau, F. Gazeau, R. H. Stauber and W. J. Parak, *Chem. Soc. Rev.*, 2016, **45**, 2440–2457.
- 33 X. Nan, Y. Huyan, H. Li, S. Sun and Y. J. C. C. R. Xu, *Coord. Chem. Rev.*, 2021, **426**, 213580.
- 34 H. Ehrlich, K. D. Demadis, O. S. Pokrovsky and P. G. Koutsoukos, *Chem. Rev.*, 2010, **110**, 4656–4689.
- 35 A. Santos, M. Sinn Aw, M. Bariana, T. Kumeria, Y. Wang and D. Losic, *J. Mater. Chem. B*, 2014, **2**, 6157–6182.
- 36 S. Mohanan, X. Guan, M. Liang, A. Karakoti and A. Vinu, *Small*, 2023, e2301113.
- 37 F. Tang, L. Li and D. Chen, *Adv. Mater.*, 2012, **24**, 1504–1534.
- 38 R. S. Guimaraes, C. F. Rodrigues, A. F. Moreira and I. J. Correia, *Pharmacol. Res.*, 2020, **155**, 104742.
- 39 P. Yang, S. Gai and J. Lin, *Chem. Soc. Rev.*, 2012, **41**, 3679–3698.
- 40 Y. Huang, P. Li, R. Zhao, L. Zhao, J. Liu, S. Peng, X. Fu, X. Wang, R. Luo, R. Wang and Z. Zhang, *Biomed. Pharmacother.*, 2022, **151**, 113053.
- 41 J. G. Croissant, K. S. Butler, J. I. Zink and C. J. Brinker, *Nat. Rev. Mater.*, 2020, **5**, 886–909.
- 42 Y. Tan, D. Yu, J. Feng, H. You, Y. Bai, J. He, H. Cao, Q. Che, J. Guo and Z. Su, *Drug Delivery Transl. Res.*, 2023, **13**, 2213–2238.
- 43 P. Mohammadi, M. Abbasinia, M. J. Assari and M. Oliaei, *Toxicol. Environ. Chem.*, 2018, **100**, 285–316.
- 44 L. Wang, M. Huo, Y. Chen and J. Shi, *Biomaterials*, 2018, **163**, 1–13.
- 45 N. Lu, P. Huang, W. Fan, Z. Wang, Y. Liu, S. Wang, G. Zhang, J. Hu, W. Liu, G. Niu, R. D. Leapman, G. Lu and X. Chen, *Biomaterials*, 2017, **126**, 39–48.
- 46 G. Yang, S. Z. F. Phua, A. K. Bindra and Y. Zhao, *Adv. Mater.*, 2019, **31**, e1805730.
- 47 J. Zhang, N. Lu, L. Weng, Z. Feng, J. Tao, X. Su, R. Yu, W. Shi, Q. Qiu, Z. Teng and L. Wang, *J. Colloid Interface Sci.*, 2021, **583**, 714–721.
- 48 Y. Zhang, Z. Teng, Q. Ni, J. Tao, X. Cao, Y. Wen, L. Wu, C. Fang, B. Wan, X. Zhang and G. Lu, *ACS Appl. Mater. Interfaces*, 2020, **12**, 57810–57820.
- 49 X. Peng, K. Chen, W. Liu, X. Cao, M. Wang, J. Tao, Y. Tian, L. Bao, G. Lu and Z. Teng, *Nano-Micro Lett.*, 2020, **12**, 137.
- 50 M. Manzano and M. Vallet-Regí, *J. Mater. Sci.*, 2018, **29**, 65.
- 51 X. Liu and J. Sun, *Biomaterials*, 2010, **31**, 8198–8209.
- 52 A. Parodi, M. Evangelopoulos, N. Arrighetti, A. Cevenini, M. Livingston, S. Z. Khaled, B. S. Brown, I. K. Yazdi, F. Paradiso, J. N. Campa-Carranza, A. De Vita, F. Taraballi and E. Tasciotti, *Small*, 2020, **16**, e1907693.
- 53 J. G. Croissant, Y. Fatieiev, A. Almalik and N. M. Khashab, *Adv. Healthcare Mater.*, 2018, **7**, 1700831.
- 54 X. Du, F. Kleitz, X. Li, H. Huang, X. Zhang and S. Z. Qiao, *Adv. Funct. Mater.*, 2018, **28**, 1707325.

- 55 M. Qiu, A. Singh, D. Wang, J. Qu, M. Swihart, H. Zhang and P. N. Prasad, *Nano Today*, 2019, **25**, 135–155.
- 56 S. Liu, S. Han, Y. Song, R. Sun, L. Zhao and C. Yan, *Adv. Healthcare Mater.*, 2023, **12**, e2300184.
- 57 Y. Hu, S. Bai, X. Wu, S. Tan and Y. J. C. I. He, *Ceram. Int.*, 2021, **47**, 31031–31041.
- 58 K. Möller and T. J. C. O. M. Bein, *Chem. Mater.*, 2019, **31**, 4364–4378.
- 59 B. Kang, M. B. Zheng, P. Song, A. P. Chen, J. W. Wei, J. J. Xu, Y. Shi and H. Y. J. S. Chen, *Small*, 2017, **13**, 1604228.
- 60 M. B. Gongalsky, A. P. Sviridov, Y. I. Bezsudnova and L. A. Osminkina, *Colloids Surf., B*, 2020, **190**, 110946.
- 61 V. Poscher and Y. Salinas, *Materials*, 2020, **13**, 3668.
- 62 B. Yang, Y. Chen and J. Shi, *Mater. Sci. Eng., R*, 2019, **137**, 66–105.
- 63 N. B. Fernandes, Y. Nayak, S. Garg and U. Y. Nayak, *Coord. Chem. Rev.*, 2023, **478**, 214977.
- 64 K. Zivojevic, M. Mladenovic, M. Djisalov, M. Mundzic, E. Ruiz-Hernandez, I. Gadjanski and N. Z. Knezevic, *J. Controlled Release*, 2021, **337**, 193–211.
- 65 L. Yu, Y. Chen, H. Lin, S. Gao, H. Chen and J. Shi, *Small*, 2018, **14**, e1800708.
- 66 L. Yu, Y. Chen, M. Wu, X. Cai, H. Yao, L. Zhang, H. Chen and J. Shi, *J. Am. Chem. Soc.*, 2016, **138**, 9881–9894.
- 67 J. Tao, Y. Tian, D. Chen, W. Lu, K. Chen, C. Xu, L. Bao, B. Xue, T. Wang, Z. Teng and L. Wang, *Angew. Chem., Int. Ed.*, 2023, **62**, e202216361.
- 68 Y. He, B. Zeng, S. Liang, M. Long and H. Xu, *ACS Appl. Mater. Interfaces*, 2017, **9**, 44402–44409.
- 69 Y. Kang, W. Sun, S. Li, M. Li, J. Fan, J. Du, X. J. Liang and X. Peng, *Adv. Sci.*, 2019, **6**, 1900716.
- 70 Y. Wang, Y. Liu, H. Wu, J. Zhang, Q. Tian and S. Yang, *Adv. Funct. Mater.*, 2019, **29**, 1805764.
- 71 V. Poscher and Y. Salinas, *Materials*, 2020, **13**, 3668.
- 72 Y. Chen and J. Shi, *Adv. Mater.*, 2016, **28**, 3235–3272.
- 73 C. Urata, H. Yamada, R. Wakabayashi, Y. Aoyama, S. Hirose, S. Arai, S. Takeoka, Y. Yamauchi and K. Kuroda, *J. Am. Chem. Soc.*, 2011, **133**, 8102–8105.
- 74 M. Giebler, S. V. Radl, M. Ast, S. Kaiser, T. Griesser, W. Kern and S. Schlögl, *J. Polym. Sci., Part A: Polym. Chem.*, 2018, **56**, 2319–2329.
- 75 B. Karimi, N. Ganji, O. Pourshiani and W. R. Thiel, *Prog. Mater. Sci.*, 2022, **125**, 100896.
- 76 M. H. Lee, Z. Yang, C. W. Lim, Y. H. Lee, S. Dongbang, C. Kang and J. S. Kim, *Chem. Rev.*, 2013, **113**, 5071–5109.
- 77 P. Zhu, Y. Chen and J. Shi, *ACS Nano*, 2018, **12**, 3780–3795.
- 78 Y. Yang, J. Wan, Y. Niu, Z. Gu, J. Zhang, M. Yu and C. Yu, *Chem. Mater.*, 2016, **28**, 9008–9016.
- 79 X. Jia, J. He, L. Shen, J. Chen, Z. Wei, X. Qin, D. Niu, Y. Li and J. Shi, *Nano Lett.*, 2019, **19**, 8690–8700.
- 80 P. Huang, Y. Chen, H. Lin, L. Yu, L. Zhang, L. Wang, Y. Zhu and J. Shi, *Biomaterials*, 2017, **125**, 23–37.
- 81 P. Yuan, H. Zhang, L. Qian, X. Mao, S. Du, C. Yu, B. Peng and S. Q. Yao, *Angew. Chem., Int. Ed.*, 2017, **56**, 12481–12485.
- 82 S. Quignard, S. Masse, G. Laurent and T. Coradin, *Chem. Commun.*, 2013, **49**, 3410–3412.
- 83 J. L. Vivero-Escoto, W. J. Rieter, H. Lau, R. C. Huxford-Phillips and W. Lin, *Small*, 2013, **9**, 3523–3531.
- 84 J. G. Croissant, C. Mauriello-Jimenez, M. Maynadier, X. Cattoen, M. Wong Chi Man, L. Raehm, O. Mongin, M. Blanchard-Desce, M. Garcia, M. Gary-Bobo, P. Maillard and J. O. Durand, *Chem. Commun.*, 2015, **51**, 12324–12327.
- 85 J. Croissant, X. Cattoen, M. W. Man, A. Gallud, L. Raehm, P. Trens, M. Maynadier and J. O. Durand, *Adv. Mater.*, 2014, **26**, 6174–6180.
- 86 E. A. Prasetyanto, A. Bertucci, D. Septiadi, R. Corradini, P. Castro-Hartmann and L. De Cola, *Angew. Chem., Int. Ed.*, 2016, **55**, 3323–3327.
- 87 Y. Lu, Y. Yang, Z. Gu, J. Zhang, H. Song, G. Xiang and C. Yu, *Biomaterials*, 2018, **175**, 82–92.
- 88 L. Yu, Y. Chen, H. Lin, W. Du, H. Chen and J. Shi, *Biomaterials*, 2018, **161**, 292–305.
- 89 D. Shao, F. Zhang, F. Chen, X. Zheng, H. Hu, C. Yang, Z. Tu, Z. Wang, Z. Chang and J. Lu, *Adv. Mater.*, 2020, **32**, 2004385.
- 90 W. Ratirotjanakul, T. Suteewong, D. Polpanich and P. Tangboriboonrat, *Microporous Mesoporous Mater.*, 2019, **282**, 243–251.
- 91 W. Zhang, H. Ma, J. Hua, W. Zhang, C. Guo and J. Wang, *J. Solid State Chem.*, 2019, **277**, 761–768.
- 92 Y. Fatiev, J. G. Croissant, K. Julfakyan, L. Deng, D. H. Anjum, A. Gurinov and N. M. Khashab, *Nanoscale*, 2015, **7**, 15046–15050.
- 93 K. M. Rao, S. Parambadath, A. Kumar, C. S. Ha and S. S. Han, *ACS Biomater. Sci. Eng.*, 2018, **4**, 175–183.
- 94 S. Zhang, Z. Chu, C. Yin, C. Zhang, G. Lin and Q. Li, *J. Am. Chem. Soc.*, 2013, **135**, 5709–5716.
- 95 G. Yang, J. Ji and Z. Liu, *Wiley Interdiscip. Rev.: Nanomed. Nanobiotechnol.*, 2021, **13**, e1720.
- 96 E. N. Arner and J. C. Rathmell, *Cancer Cell*, 2023, **41**, 421–433.
- 97 F. Chen, X. Zhuang, L. Lin, P. Yu, Y. Wang, Y. Shi, G. Hu and Y. Sun, *BMC Med.*, 2015, **13**, 45.
- 98 Y. Yang, H. Wu, B. Liu and Z. Liu, *Adv. Drug Delivery Rev.*, 2021, **179**, 114004.
- 99 Y. Zhang, I. Kim, Y. Lu, Y. Xu, D. G. Yu and W. Song, *J. Controlled Release*, 2022, **349**, 963–982.
- 100 T. Su, S. Huang, Y. Zhang, Y. Guo, S. Zhang, J. Guan, M. Meng, L. Liu, C. Wang, D. Yu, H. Y. Kwan, Z. Huang, Q. Huang, E. Lai-Han Leung, M. Hu, Y. Wang, Z. Liu and L. Lu, *Acta Pharm. Sin. B*, 2022, **12**, 821–837.
- 101 R. Zhang, T. Liu, W. Li, Z. Ma, P. Pei, W. Zhang, K. Yang and Y. Tao, *J. Nanobiotechnol.*, 2022, **20**, 223.
- 102 S. Chen, M. Chen, J. Yang, X. Zeng, Y. Zhou, S. Yang, R. Yang, Q. Yuan and J. Zheng, *Small*, 2021, **17**, e2100243.
- 103 H. Omar, J. G. Croissant, K. Alamoudi, S. Alsaiani, I. Alradwan, M. A. Majrashi, D. H. Anjum, P. Martins, R. Laamarti, J. Eppinger, B. Moosa, A. Almalik and N. M. Khashab, *J. Controlled Release*, 2017, **259**, 187–194.
- 104 T. Liu, M. Zhu, X. Chang, X. Tang, P. Yuan, R. Tian, Z. Zhu, Y. Zhang and X. Chen, *Adv. Mater.*, 2023, **35**, e2300086.

- 105 L. Dai, X. Li, X. Duan, M. Li, P. Niu, H. Xu, K. Cai and H. Yang, *Adv. Sci.*, 2019, **6**, 1801807.
- 106 C. Li, Y. Wang, Y. Du, M. Qian, H. Jiang, J. Wang, N. Murthy and R. Huang, *Biomaterials*, 2018, **186**, 1–7.
- 107 S.-Y. Peng, M.-Z. Zou, C.-X. Zhang, J.-B. Ma, X. Zeng and W. Xiao, *J. Drug Delivery Sci. Technol.*, 2020, **55**, 101450.
- 108 J. Wu, D. H. Bremner, S. Niu, H. Wu, J. Wu, H. Wang, H. Li and L.-M. Zhu, *Chem. Eng. J.*, 2018, **342**, 90–102.
- 109 R. Cheng, F. Feng, F. Meng, C. Deng, J. Feijen and Z. Zhong, *J. Controlled Release*, 2011, **152**, 2–12.
- 110 M. Wu, Q. Meng, Y. Chen, Y. Du, L. Zhang, Y. Li, L. Zhang and J. Shi, *Adv. Mater.*, 2015, **27**, 215–222.
- 111 Z. Zheng, Z. Jia, C. Qu, R. Dai, Y. Qin, S. Rong, Y. Liu, Z. Cheng and R. Zhang, *Small*, 2021, **17**, e2006508.
- 112 M. Wei, J. Bai, X. Shen, K. Lou, Y. Gao, R. Lv, P. Wang, X. Liu and G. Zhang, *ACS Nano*, 2023, **17**, 11345–11361.
- 113 W. Guo, Z. Chen, J. Chen, X. Feng, Y. Yang, H. Huang, Y. Liang, G. Shen, Y. Liang, C. Peng, Y. Li, G. Li, W. Huang, B. Zhao and Y. Hu, *J. Nanobiotechnol.*, 2020, **18**, 99.
- 114 H. Lu, S. Xu, G. Ge, Z. Guo, M. Zhao and Z. Liu, *ACS Appl. Mater. Interfaces*, 2022, **14**, 44098–44110.
- 115 F. Zhang, F. Chen, C. Yang, L. Wang, H. Hu, X. Li, X. Zheng, Z. Wang, Z. Chang, T. Li, L. Li, M. Ge, J. Du, W. Sun, W. F. Dong and D. Shao, *Small*, 2021, **17**, e2100006.
- 116 L. Li, J. Zou, Y. Dai, W. Fan, G. Niu, Z. Yang and X. Chen, *Nat. Biomed. Eng.*, 2020, **4**, 1102–1116.
- 117 B. Liu, S. Liang, Z. Wang, Q. Sun, F. He, S. Gai, P. Yang, Z. Cheng and J. Lin, *Adv. Mater.*, 2021, **33**, e2101223.
- 118 Z. Chen, F. Han, Y. Du, H. Shi and W. Zhou, *Signal Transduction Targeted Ther.*, 2023, **8**, 70.
- 119 P. Lee, N. S. Chandel and M. C. Simon, *Nat. Rev. Mol. Cell Biol.*, 2020, **21**, 268–283.
- 120 K. Tang, X. Li, Y. Hu, X. Zhang, N. Lu, Q. Fang, J. Shao, S. Li, W. Xiu, Y. Song, D. Yang and J. Zhang, *Biomater. Sci.*, 2023, **11**, 4411–4429.
- 121 J. Zhang, K. Tang, R. Fang, J. Liu, M. Liu, J. Ma, H. Wang, M. Ding, X. Wang, Y. Song and D. Yang, *Front. Pharmacol.*, 2023, **14**, 1140362.
- 122 M. Z. Zou, W. L. Liu, H. S. Chen, X. F. Bai, F. Gao, J. J. Ye, H. Cheng and X. Z. Zhang, *Natl. Sci. Rev.*, 2021, **8**, nwa160.
- 123 J. N. Liu, W. Bu and J. Shi, *Chem. Rev.*, 2017, **117**, 6160–6224.
- 124 S. Chen, J. Liu, Y. Li, X. Wu, Q. Yuan, R. Yang and J. Zheng, *TrAC, Trends Anal. Chem.*, 2020, **131**, 116010.
- 125 H. B. Cheng, S. Zhang, J. Qi, X. J. Liang and J. Yoon, *Adv. Mater.*, 2021, **33**, e2007290.
- 126 J. Zhu, T. Guo, Z. Wang and Y. Zhao, *J. Controlled Release*, 2022, **345**, 475–493.
- 127 Q. Tian, Y. Li, S. Jiang, L. An, J. Lin, H. Wu, P. Huang and S. Yang, *Small*, 2019, **15**, e1902926.
- 128 G. Shim, Q. V. Le, J. Suh, S. Choi, G. Kim, H. G. Choi, Y. B. Kim, R. B. Macgregor, Jr. and Y. K. Oh, *J. Controlled Release*, 2019, **298**, 110–119.
- 129 X. Jiang, X. Fan, W. Xu, C. Zhao, H. Wu, R. Zhang and G. Wu, *J. Controlled Release*, 2019, **316**, 196–207.
- 130 J. Fu, L. Liu, Z. Huang, Y. Lai, H. Ji, S. Peng, J. Tian and Y. Zhang, *J. Med. Chem.*, 2013, **56**, 4641–4655.
- 131 W. H. Chen, G. F. Luo, Q. Lei, S. Hong, W. X. Qiu, L. H. Liu, S. X. Cheng and X. Z. Zhang, *ACS Nano*, 2017, **11**, 1419–1431.
- 132 X. Dong, W. Yin, X. Zhang, S. Zhu, X. He, J. Yu, J. Xie, Z. Guo, L. Yan, X. Liu, Q. Wang, Z. Gu and Y. Zhao, *ACS Appl. Mater. Interfaces*, 2018, **10**, 4271–4284.
- 133 H. Gong, Y. Chao, J. Xiang, X. Han, G. Song, L. Feng, J. Liu, G. Yang, Q. Chen and Z. Liu, *Nano Lett.*, 2016, **16**, 2512–2521.
- 134 J. G. Croissant, Y. Fatieiev, K. Julfakyan, J. Lu, A.-H. Emwas, D. H. Anjum, H. Omar, F. Tamanoi, J. I. Zink and N. M. Khashab, *Chem. – Eur. J.*, 2016, **22**, 14806–14811.
- 135 N. Qiu, X. Liu, Y. Zhong, Z. Zhou, Y. Piao, L. Miao, Q. Zhang, J. Tang, L. Huang and Y. Shen, *Adv. Mater.*, 2016, **28**, 10613–10622.
- 136 P. Shen, X. Zhang, N. Ding, Y. Zhou, C. Wu, C. Xing, L. Zeng, L. Du, J. Yuan and Y. Kang, *ACS Appl. Mater. Interfaces*, 2023, **15**, 20697–20711.
- 137 R. Zhang, S. Shao, Y. Piao, J. Xiang, X. Wei, Z. Zhang, Z. Zhou, J. Tang, N. Qiu, X. Xu, Y. Liu and Y. Shen, *Adv. Mater.*, 2023, e2303614, DOI: [10.1002/adma.202303614](https://doi.org/10.1002/adma.202303614).
- 138 N. H. Tsao and E. A. Hall, *Langmuir*, 2016, **32**, 6534–6543.
- 139 X. Li, Y. Chen, X. Zhang and Y. Zhao, *Mater. Sci. Eng., C*, 2020, **112**, 110914.
- 140 Y. Zhang, L. Liu, W. Li, C. Zhang, T. Song, P. Wang, D. Sun, X. Huang, X. Qin, L. Ran, G. Tian, J. Qian and G. Zhang, *J. Nanobiotechnol.*, 2023, **21**, 9.
- 141 J. L. Li, Y. J. Cheng, C. Zhang, H. Cheng, J. Feng, R. X. Zhuo, X. Zeng and X. Z. Zhang, *ACS Appl. Mater. Interfaces*, 2018, **10**, 5287–5295.
- 142 X. Li, X. Zhang, Y. Zhao and L. Sun, *J. Inorg. Biochem.*, 2020, **202**, 110887.
- 143 Y. Yang, Y. Lu, P. L. Abbaraju, I. Azimi, C. Lei, J. Tang, M. Jambhrunkar, J. Fu, M. Zhang, Y. Liu, C. Liu and C. Yu, *Adv. Funct. Mater.*, 2018, **28**, 1800706.
- 144 X. Jia, Y. Zhang, Y. Zou, Y. Wang, D. Niu, Q. He, Z. Huang, W. Zhu, H. Tian, J. Shi and Y. Li, *Adv. Mater.*, 2018, **30**, e1704490.
- 145 A. Sharma, J. F. Arambula, S. Koo, R. Kumar, H. Singh, J. L. Sessler and J. S. Kim, *Chem. Soc. Rev.*, 2019, **48**, 771–813.
- 146 Y. Li, L. Zhao and X. F. Li, *Front. Oncol.*, 2021, **11**, 700407.
- 147 D. Cheng, Y. Ji, B. Wang, T. Jin, Y. Xu, X. Qian and W. Zhu, *Int. J. Pharm.*, 2021, **603**, 120730.
- 148 T. Yin, J. Liu, Z. Zhao, Y. Zhao, L. Dong, M. Yang, J. Zhou and M. Huo, *Adv. Funct. Mater.*, 2017, **27**, 1604620.
- 149 Y. Zhong, K. Goltsche, L. Cheng, F. Xie, F. Meng, C. Deng, Z. Zhong and R. Haag, *Biomaterials*, 2016, **84**, 250–261.
- 150 H. Birkedal-Hansen, W. G. Moore, M. K. Boddien, L. J. Windsor, B. Birkedal-Hansen, A. DeCarlo and J. A. Engler, *Crit. Rev. Oral Biol. Med.*, 1993, **4**, 197–250.
- 151 M. Egeblad and Z. Werb, *Nat. Rev. Cancer*, 2002, **2**, 161–174.
- 152 B. Yang, H. Fu, R. Kong, G. Zheng, X. Wang, Y. Dong and Z. Yang, *J. Mater. Chem. B*, 2022, **10**, 8490–8501.

- 153 S. J. Park, W. Ye, R. Xiao, C. Silvin, M. Padget, J. W. Hodge, C. Van Waes and N. C. Schmitt, *Oral Oncol.*, 2019, **95**, 127–135.
- 154 Y. Shi, M. Zhou, Y. Zhang, Y. Wang and J. Cheng, *Acta Biomater.*, 2023, **158**, 571–582.
- 155 Y. Fang, X. Luo, Y. Xu, Z. Liu, R. L. Mintz, H. Yu, X. Yu, K. Li, E. Ju, H. Wang, Z. Tang, Y. Tao and M. Li, *Adv. Sci.*, 2023, **10**, e2300899.
- 156 D. Cao, L. Chen, Z. Zhang, Y. Luo, L. Zhao, C. Yuan, J. Lu, X. Liu and J. Li, *J. Mater. Chem. B*, 2023, **11**, 1829–1848.
- 157 K. Kessenbrock, V. Plaks and Z. Werb, *Cell*, 2010, **141**, 52–67.
- 158 L. Claesson-Welsh, *J. Clin. Invest.*, 2020, **130**, 1093–1095.
- 159 A. R. Nelson, B. Fingleton, M. L. Rothenberg and L. M. Matrisian, *J. Clin. Oncol.*, 2000, **18**, 1135–1149.
- 160 Y. C. Chan and M. Hsiao, *Nanomedicine*, 2017, **12**, 2153–2159.
- 161 J. Li, Z. Ge, K. Toh, X. Liu, A. Dirisala, W. Ke, P. Wen, H. Zhou, Z. Wang, S. Xiao, J. F. R. Van Guyse, T. A. Tockary, J. Xie, D. Gonzalez-Carter, H. Kinoh, S. Uchida, Y. Anraku and K. Kataoka, *Adv. Mater.*, 2021, **33**, e2105254.
- 162 R. Xiao, J. Ye, X. Li and X. Wang, *Int. J. Biol. Macromol.*, 2023, **238**, 124032.
- 163 Y. Hu, S. Bai, X. Fan, F. Zhou, B. Chen, S. Tan, H. Xu, A. Pan, S. Liang and Y. He, *Biomater. Sci.*, 2022, **10**, 2358–2369.
- 164 S. Yan, P. Sun, N. Niu, Z. Zhang, W. Xu, S. Zhao, L. Wang, D. Wang and B. Z. Tang, *ACS Nano*, 2022, **16**, 9785–9798.
- 165 M. Wang, W. Zhang, B. Ding, P. A. Ma and J. Lin, *Adv. Opt. Mater.*, 2023, **11**, 2202040.